

Ice XIX: The second hydrogen-ordered polymorph related to ice VI

Tobias Gasser

University of Innsbruck

Alexander Thoeny

University of Innsbruck

Andrew Fortes

Rutherford Appleton Laboratory <https://orcid.org/0000-0001-5907-2285>

Thomas Loerting (✉ thomas.loerting@uibk.ac.at)

University of Innsbruck <https://orcid.org/0000-0001-6694-3843>

Article

Keywords: Ice XIX, hydrogen-ordered polymorph, ice VI, ice polymorph

Posted Date: October 7th, 2020

DOI: <https://doi.org/10.21203/rs.3.rs-86075/v1>

License: © ⓘ This work is licensed under a Creative Commons Attribution 4.0 International License.

[Read Full License](#)

Version of Record: A version of this preprint was published at Nature Communications on February 18th, 2021. See the published version at <https://doi.org/10.1038/s41467-021-21161-z>.

Ice XIX: The second hydrogen-ordered polymorph related to ice VI

Tobias M. Gasser¹, Alexander V. Thoeny¹, A. Dominic Fortes², Thomas Loerting^{1,*}

¹*Institute of Physical Chemistry, University of Innsbruck, 6020 Innsbruck, Austria*

²*ISIS Neutron and Muon Facility, Rutherford Appleton Laboratory, Harwell Science and Innovation Campus, Chilton, Oxfordshire, OX11 0QX, UK*

e-mail: thomas.loerting@uibk.ac.at

Abstract:

We here report *ex situ* calorimetry and high-resolution neutron powder diffraction data of a novel ice polymorph produced at 1.8 GPa and recovered to ambient pressure at 80 K. Ice XIX, previously called ice β -XV by us, is shown to be partially hydrogen-ordered and crystallising in a $\sqrt{2} \times \sqrt{2} \times 1$ supercell with respect to the parent ice VI phase. Our powder data match two nearly degenerate structural models in space-groups $P\bar{4}$ and $Pcc2$, in which the water molecules are partially antiferroelectrically ordered. Key to the synthesis of deuterated ice XIX is the use of DCl as dopant and the use of a D₂O/H₂O mixture, where the small H₂O fraction nucleates ice XIX. This provides the basis to study the first order-order transition known in ice physics, from ice XIX to its sibling ice XV at ambient pressure. It proceeds *via* a transition state, ice VI[‡], which contains a disordered H-sublattice, whereas both ice XIX and ice XV are fully crystalline.

Introduction

Hexagonal ice (ice I_h), familiar to most of us from snow or the freezer, is a geometrically frustrated ice. While the oxygen atoms fully occupy crystallographic sites in the molecular framework, the hydrogen atoms are disordered over partially-occupied sites. Yet, the Bernal-Fowler rules¹, also known as the ice rules, are obeyed, in the sense that (i) the crystal is composed of H_2O molecules and (ii) there is always a single hydrogen atom between two oxygen atoms, so that a space-filling hydrogen-bonded network is formed. Following these rules many different configurations are allowed, where the total number of possible microstates gives rise to a configurational entropy S_{conf} of approximately $S_{conf} = R \ln(3/2)$ known as Pauling entropy². Below the order-disorder temperature T_{o-d} thermodynamics requires a fully ordered phase to be more stable than this frustrated ice. In this phase both H and O atoms are ordered, so that the configurational entropy is zero. How the H atoms order and the net dipole moment of the ordered structure are a challenge to predict accurately. Quite often the ordered ice is not accessible through simple cooling. In case of ice I_h T_{o-d} was found to be very low, at 72 K³⁻⁵ – and yet, even upon cooling ice I_h slowly below 72 K it does not order. The times required for order to develop are simply beyond laboratory time scales. Only in 1972 Kawada³ achieved the transition, where applying two key concepts allowed access to the ordered ice⁶: (i) nucleation of the ordered phase by keeping the sample for a few days about 10 K below T_{o-d} , (ii) accelerated growth of the ordered ice phase through the use of extrinsic defects just below T_{o-d} . Specifically, Kawada was the first to use KOH doping, which generates an ionic OH^- defect (violating ice rule (i)) together with a Bjerrum-L-defect (violating ice rule (ii))⁷. Such defects are now known to accelerate the reorientational dynamics by up to five orders of magnitude⁸. The ordered phase related to ice I_h that needs growth times of a few days is now known as ice XI. Ice XI represents the ground state of ice at 0 K and ambient pressure, not ice I_h or ice II as previously believed⁹. Its ferroelectric ordering determined from single crystal neutron diffraction data⁶ and molecular simulations¹⁰ has been challenged and subsequently claimed to be antiferroelectric¹¹. The same issues arise for a plethora of high-pressure ice phases. For instance, disordered ice V and ice XII, could only be transformed to their ordered counterparts, ice XIII and ice XIV, through the use of HCl doping¹². HCl doping introduces an ionic H_3O^+ defect, together with a Bjerrum-L-defect. In these cases T_{o-d} is 112 ± 3 K^{8,12-15} and 102 ± 3 K^{12,14,16-18}, respectively. Their growth takes place on the time scale of hours rather than days because of the higher T_{o-d} . Undoped or KOH-doped ices do not order sufficiently fast, for reasons that are yet not fully understood. The ice III/IX and ice VII/VIII order-disorder pairs have T_{o-d} s of 170 K and 273 K⁷, respectively – high enough so that the use of dopants is no longer necessary to achieve ordering.

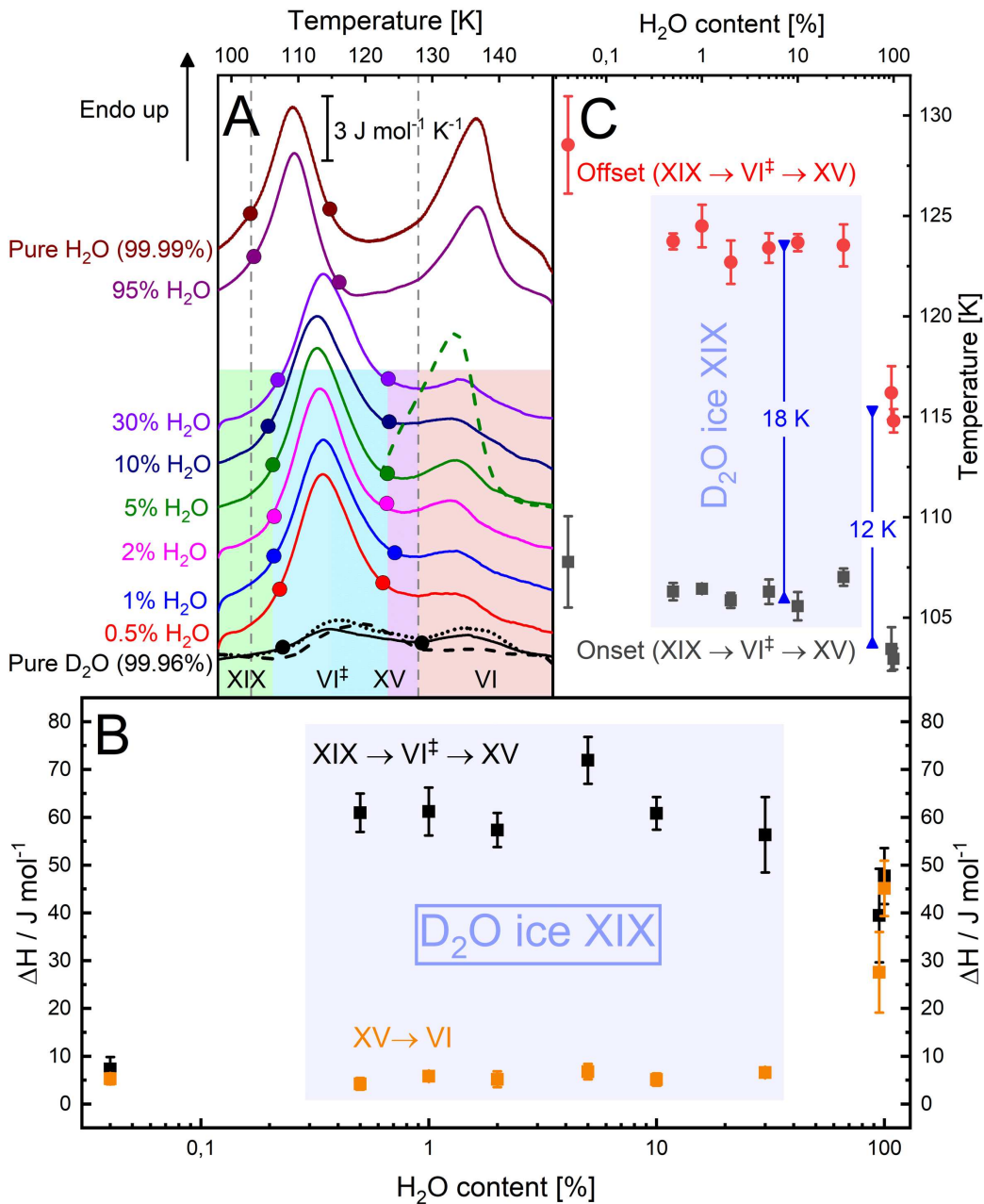
A particularly challenging and interesting case is disordered ice VI. Antiferroelectrically ordered ice XV forms upon cooling, again, only in the presence of acid doping¹⁹. In earlier work, without the use of a dopant, only a very slow ordering process could be inferred²⁰. Its T_{o-d} has been determined to be 129 ± 2 K^{19,21-24}. Yet, much more complex kinetics than in other ice phases has been recognized, with a low-temperature tail extending to as low as 100 K²⁵. This has already been a hint to the existence of a competing ordering process, even though not recognized as such at the time²⁵. The transition is also clearly affected by the choice of pressure. The ordering process to yield ice XV seems to be impeded at high-pressures, but alleviated at ambient pressure. In 2018 some of us have claimed that the ordering process to ice XV is not only slowed down severely near 2 GPa, but instead a transition to a differently-ordered phase takes over²³. This ordering process leads to a phase called ice β -XV by us, where T_{o-d} for ice VI/ β -XV was shown to be about 26 K below the T_{o-d} for ice VI/XV²³. In other words, the low temperature tail recognized first by Shephard & Salzmann²⁵ originates from the transition of remaining ice VI to ice β -XV. Supporting this hypothesis, calorimetry experiments have shown that two disordering processes take place upon heating ice β -XV²³. Both ice β -XV and ice XV only release a small fraction of the entropy expected for the transition from a fully ordered to a fully

disordered state. In other words, calorimetry suggests both polymorphs to be weakly ordered variants of ice VI²³. For ice XV this claim has already been crystallographically demonstrated¹⁹, while for ice β -XV crystallographic analysis has so far remained elusive. Another key experiment to make the case for the presence of two distinct ordered phases is dielectric relaxation spectroscopy, which shows the activation energy for dielectric relaxation as 45 kJ/mol in ice β -XV, but only 27 kJ/mol in ice XV²³. Raman spectroscopy reveals clear differences between ices VI, XV and β -XV, e.g., in the librational and OH-stretching regions²⁴. Some of us have previously argued that an unfavourably large kinetic isotope effect hampers formation of deuterated ice β -XV²³, the deuterated analogue being required for accurate determination of hydrogen site ordering using neutron powder diffraction. The same slow cooling process that allows H₂O ice β -XV to form from H₂O ice VI just does not allow D₂O ice β -XV to form from D₂O ice VI. The lack of an experimental crystal structure for ice β -XV has led to widespread speculations about its nature. Whereas Rosu-Finsen & Salzmann have argued for ice β -XV to be in fact a disordered state, in which the H atoms are immobile, i.e., a deep glassy state^{26,27}, some of us have speculated about a crystalline phase with a ferroelectric nature²³.

We here show that in fact *growth* of deuterated ice β -XV is not at the origin of the large isotope effect. Instead, *nucleation* of deuterated ice β -XV in ice VI is the limiting step. Our key result is that nucleation of protiated ice β -XV helps growth of deuterated ice β -XV. Adding only 0.5% of H₂O to pure D₂O allows for the formation of D₂O ice β -XV. Using samples containing a small fraction of water, and DCl as dopant, we provide neutron powder diffraction data and determine its crystal structure. For this reason ice β -XV can now be renamed as ice XIX, following the recent discovery of superionic ice XVIII²⁸. The ice XIX to ice XV transition incurred upon heating represents the first order-to-order transition in the H-sublattice known in any kind of water ice.

Results

Figure 1: (A) Differential scanning calorimetry scans of ice XIX samples with different D_2O/H_2O ratios recorded at a heating rate of 10 K/min. The two endotherms indicate first the ice $XIX \rightarrow VI^\ddagger \rightarrow XV$ and second the ice $XV \rightarrow VI$ transition. All full lines were recorded on samples slow-cooled at 1.8 GPa (see Methods). Dashed lines mark heating scans of ice XIX annealed at 1.8 GPa and 106 K (black dashed line, pure D_2O) and annealed at ambient pressure and 120 K (green dashed line, 5% H_2O). Heating scan of ice XIX after very slow cooling at 1.8 GPa is shown as dotted black line (pure D_2O). Onset and offset points for the first transition are marked by full circles. (B) Enthalpy changes associated with the two transitions (black squares: $XIX \rightarrow VI^\ddagger \rightarrow XV$; orange squares: $XV \rightarrow VI$). (C) Onset (black squares) and offset points (red circles). Error bars reflect both reproducibility and ambiguities in determining the points based on the tangent method. The width of the transition at 10 K/min is indicated through the blue double arrow.

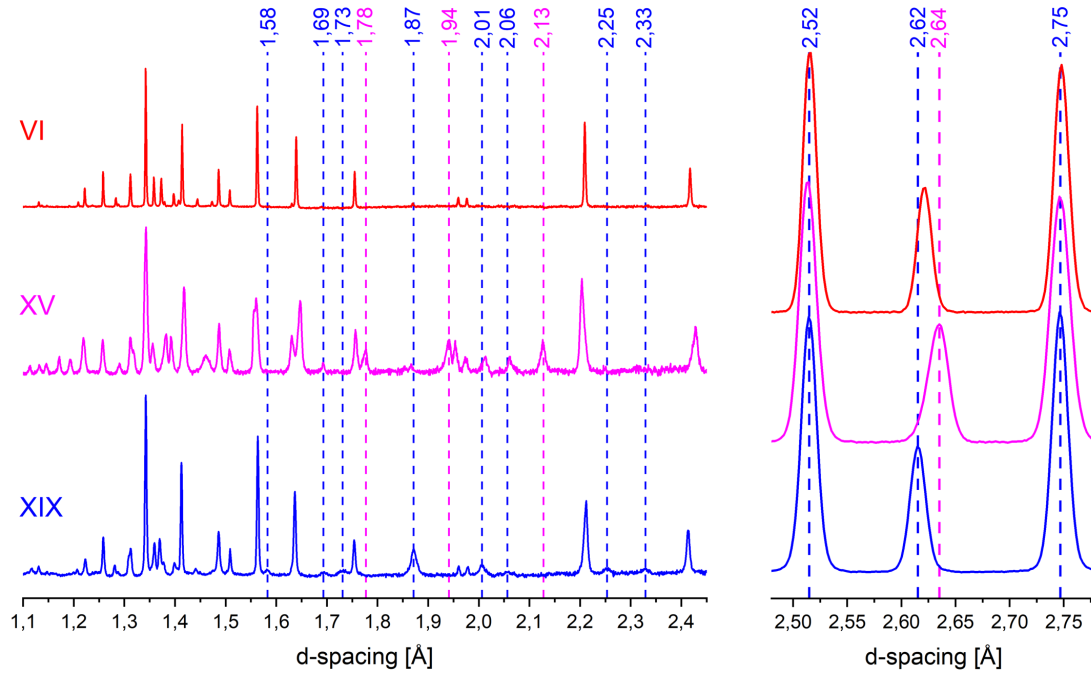


Calorimetry: nucleation of H₂O ice XIX and growth of D₂O ice XIX

Figure 1 shows ambient pressure calorimetry scans for H₂O, D₂O and mixed D₂O/H₂O samples. The samples were consistently made by cooling the liquid to 77 K at ambient pressure, then subjecting the frozen material to pressure. At 1.8 GPa the samples were first heated to 255 K and finally cooled back to 77 K very slowly. For pure H₂O samples this procedure has been shown to result in the formation of ice β -XV in our previous work²³. The calorimetry trace for pure H₂O (top trace in Figure 1A) shows two well separated endotherms, where the first one indicates disordering of ice β -XV and the second one indicates disordering of ice XV, resulting in ice VI. As indicated in Figure 1B both endotherms are approximately the same size of 50 J/mol, in agreement with our earlier work (Figure 2 in ref. 23). Considering the difference of 25 K in T_{o-d} for these two endotherms this corresponds to a loss of S_{conf} of 0.46 and 0.35 Jmol⁻¹K⁻¹ in pure H₂O samples, respectively. For pure D₂O the exact same procedure results in the trace depicted at the bottom of Figure 1A. In spite of the large magnification used in Figure 1A (see scale bar) there are hardly any features different from the baseline. Yet, two very subtle endotherms (close to the resolution limit of the instrument) can be identified, both of which are less than 10 J/mol. That is, the bulk of the sample had remained disordered ice VI upon cooling under pressure. This had prevented neutron diffraction work on the crystal structure before the present study. In order to resolve the issue we have first attempted to reduce the cooling rate significantly below 3 K/min, which is the rate that successfully produces H₂O ice β -XV. The lowest cooling rate employed for D₂O samples was 0.1 K/min, thereby providing 13 hours for the sample to order upon cooling. Even reduction of the cooling rate by this factor of 30 has not changed the picture, where still barely any ordering takes place upon cooling D₂O ice VI (see black dotted trace in Figure 1A). Furthermore, we have attempted to isothermally keep the sample below the T_{o-d} of ice β -XV for 25 hours. As mentioned above, this strategy has proven to be successful to generate ice XI from ice I_h. The black, dashed calorimetry trace at the bottom of Figure 1A, however, shows that also this strategy has not resulted in D₂O ice β -XV.

The mere fact that reducing the cooling rate still does not increase the order within the ice VI sample points against phase *growth* as the issue. Instead *nucleation* of D₂O ice β -XV is inhibited and the limiting factor that needs to be tackled to prepare the deuterated polymorph. We know from our previous work that H₂O ice β -XV successfully nucleates within ice VI²³. Thus, we have attempted to grow D₂O ice β -XV on top of H₂O ice β -XV nuclei. The result of adding purposefully H₂O to D₂O samples is summarized in Figure 1A, for samples containing between 0.5% and 95% of H₂O. Already 0.5% makes a tremendous difference. The disordering endotherm near 100 K suddenly appears with an enthalpy of 61 J/mol. Repeating the experiment with 1%, 2%, 5%, 10% or even 30% added H₂O barely changes this picture. Only for the 95% H₂O sample the calorimetry traces of pure H₂O are restored. This suggests that our strategy has been successful, i.e., that D₂O ice β -XV has grown starting from H₂O ice β -XV nuclei. This is confirmed when inspecting isotope effects on the latent heat and disordering temperature. The enthalpy associated with disordering of D₂O ice β -XV is about 64±8 J/mol as compared to 45±5 J/mol for the case of H₂O ice β -XV – a typical isotope effect for endotherms. The onset point for the D₂O sample shifts to higher temperatures by about 3 K – again a quite typical isotope effect^{18,29}. That is, the DSC traces suggest that D₂O ice β -XV indeed does form in all mixtures containing from 0.5% to 30% H₂O. For this reason these compositions are coloured in blue and marked D₂O ice XIX in Figure 1B/C. In the Supporting Information we show why the second endotherm (ice XV→ice VI) in Figure 1A is much smaller in deuterated than protiated samples. In brief, this reflects that the formation of ice XV is much slower in deuterated samples, as seen from the larger width of the first endotherm (18 K vs. 12 K, see blue arrow in Figure 1C). This implies that the transition from ice XIX to ice XV proceeds through a disordered transition state, called ice VI[‡] here.

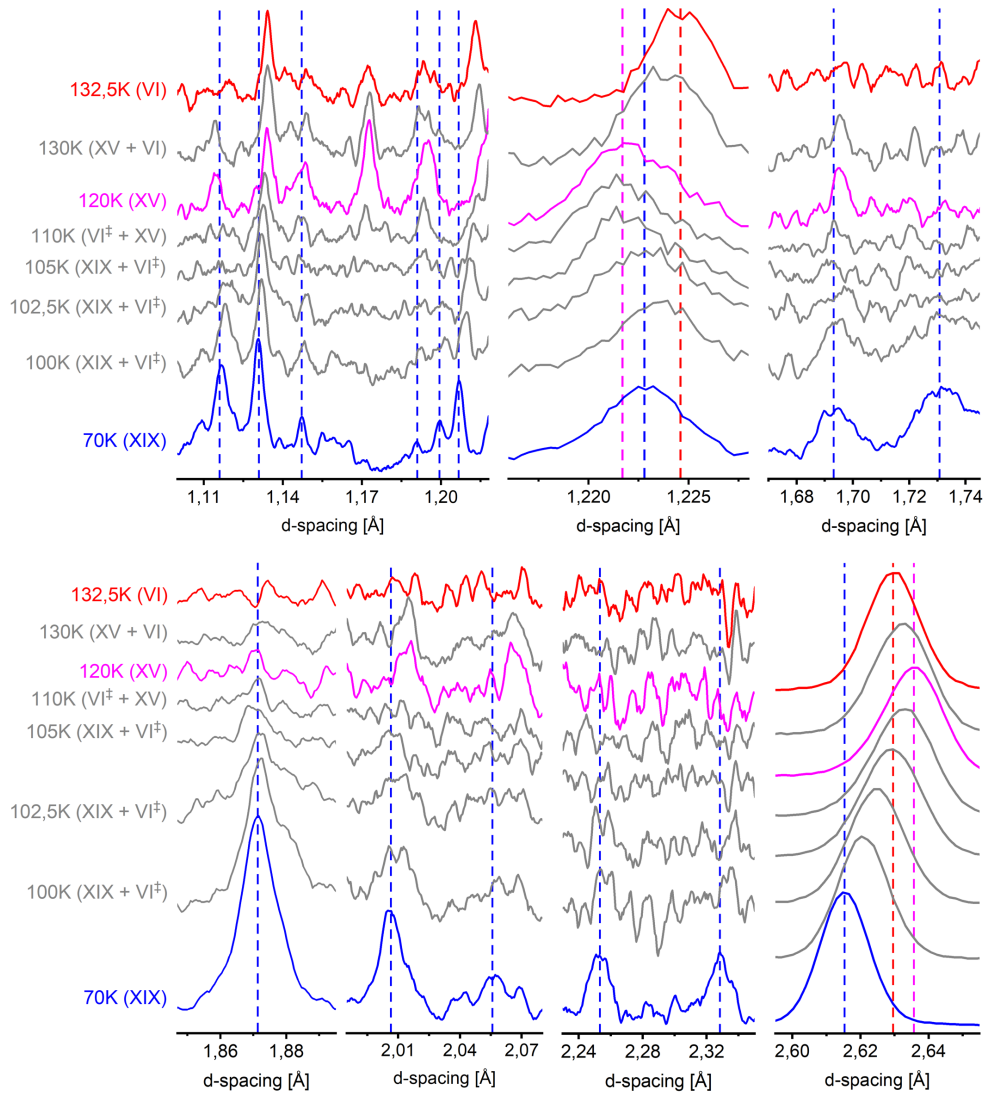
Figure 2: Comparison of ice XIX, ice XV and ice VI neutron powder diffraction patterns. Baselines were corrected with an 8 pt spline. Selected features of the ice XIX and ice XV diffractograms are highlighted by vertical, dashed blue and magenta lines, respectively. Note the sharp peaks in ice VI and the broader peaks in ices XV and XIX – this hints at particle size broadening from very small partially ordered domains. The diffractograms on the left were acquired in HRPD’s highest resolution backscattering banks ($2\theta = 165\pm 11^\circ$) whilst the three peaks shown on the right were recorded in the medium-resolution detectors at $2\theta = 90\pm 10^\circ$.



Neutron powder diffraction: comparing ice VI, XV and ice XIX

Let us now turn to the neutron powder diffraction measurements of the deuterated samples on the High Resolution Powder Diffractometer, HRPD, at the ISIS spallation neutron source. We recorded data out to 10 Å and used the highest-resolution data in the backscattering banks at d-spacings from 0.65 to 2.60 Å for structure refinements. Figure 2 compares the powder diffraction patterns for undoped ice VI, ice XV and ice β -XV, all recorded on HRPD. The *ex situ* neutron diffraction pattern of ice VI recorded at 80 K under ~50 mbar of He exchange gas matches very well with the known pattern, as measured *in situ* at 225 K and 1.1 GPa by Kuhs et al.³⁰ or *ex situ* by Salzmänn et al.¹⁹ on the GEM instrument. It also matches the tetragonal $P4_2/nmc$ structure deduced by Kamb in 1965 from X-ray measurements³¹. The ice XV pattern recorded from a sample recooled from 135 K with a cooling rate of 0.4 K/min at 50 mbar matches nicely with the pattern recorded by Salzmänn et al.¹⁹. Compared to ice VI, new Bragg peaks at 1.775, 1.938, 2.013, 2.066 and 2.129 Å are found in the ice XV pattern¹⁹. The ice β -XV pattern recorded from a sample containing 5% H₂O is depicted at the bottom of Figure 2. This pattern is different from both the ice XV and the ice VI patterns. Eight Bragg reflexes at d-spacings between 1.5 and 2.4 Å are marked by blue dashed lines that appear in ice β -XV, but not in ice VI. The 1.583, 1.734, 2.254 and 2.326 Å features also do not appear in ice XV. The 1.775, 1.938 and 2.129 Å features characteristic of ice XV on the other hand do not appear in ice β -XV (see dashed, magenta lines in Figure 2). Also the shift of the intense feature from 2.64 Å in ice XV to 2.62 Å in ice β -XV is noteworthy. That is, the ice β -XV pattern is different from ice XV and ice VI, in spite of sharing the same kind of oxygen network. Note that the Bragg peaks observed in backscattering from ice VI are substantially sharper than in either ice XV or ice β -XV. This appears to be the result of particle-size broadening in the latter two phases, most likely due to the development of many small domains ordering upon cooling ice VI. Below we show the behaviour upon heating in HRPD and the refinement of the recorded data, which makes the case for ice β -XV being renamed to ice XIX.

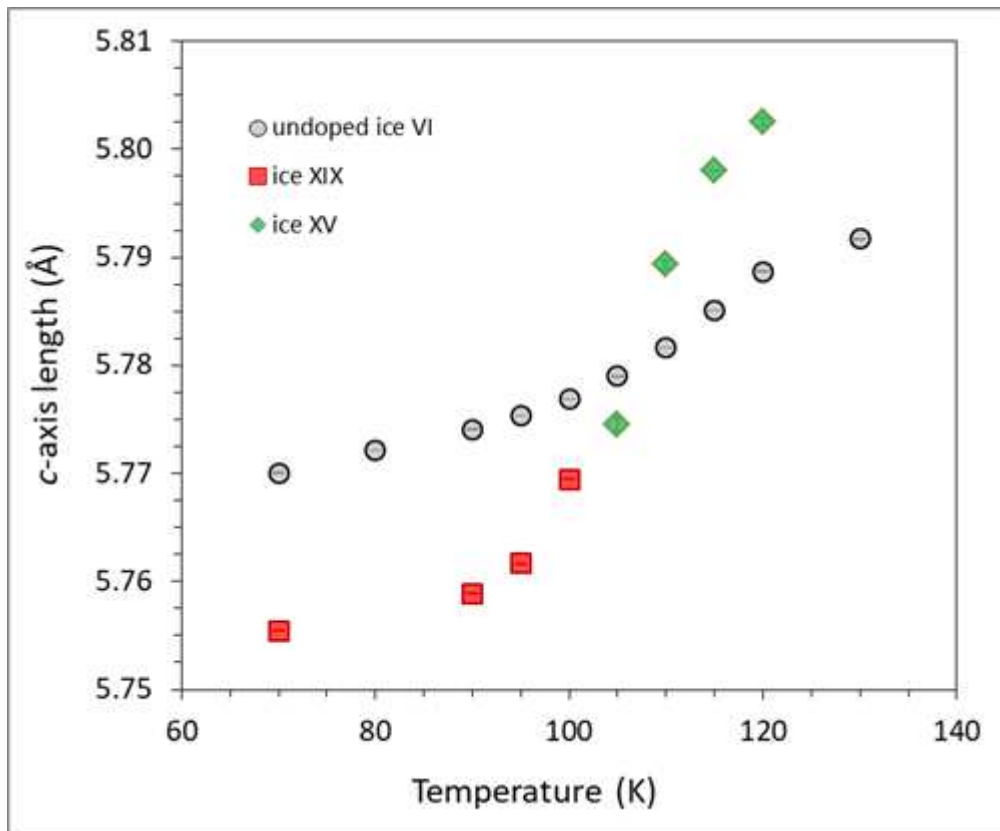
Figure 3: Heating of a D_2O ice XIX sample in HRPD, revealing transitions to ice XV (120K) (via ice VI^\ddagger) and to ice VI (132.5K). Data in Panel 1, 3, 4, 5 and 6 were smoothed using a 13pt Savitzky-Golay.



Order-order transition ice XIX → ice XV based on neutron powder diffraction

The phase behaviour upon heating ice XIX from 70 to 132.5 K is demonstrated in Figure 3 for seven selected marker regions. To aid the eye blue, pink and red dashed lines are used to indicate marker bands for ice XIX, ice XV and ice VI, respectively. Let's first inspect the 1.69 and 1.73 Å features characteristic of ice XIX (blue in Figure 3). They are well resolved at 70 K, and still well resolved at 100 K. At 102.5 K these two features shrink in intensity and then disappear at 105 K. At 105 K the pattern is practically featureless, as is the case in ice VI. Upon continued heating the feature at 1.69 Å reappears (slightly shifted), but the one at 1.73 Å does not. This trend continues until 120 K, where the 1.69 Å reflex is nicely developed. This pattern is characteristic of ice XV (pink in Figure 3). Upon further heating this peak disappears again, and has fully vanished at 132.5 K, at which temperature ice VI (red in Figure 3) is developed. At all other temperatures the patterns are depicted in grey to indicate that at least two phases contribute to the diffraction signal. The shift of the reflex at 1.22 Å is also quite revealing. Compared to 70 K the peak first upshifts at 102.5 K, close to its position in ice VI. That is, ice XIX first disorders, producing ice VI[‡]. On continued heating the feature downshifts again, finally reaching the ice XV position at 120 K. That is, between 102.5 K and 120 K ordering of ice XV takes place starting from transient ice VI[‡]. In the diffraction experiment the ordering reaches completion because many hours are available for the process, as opposed to the calorimetry experiment in Figure 1A providing only 2.5 minutes. Above 120 K the position upshifts again, reaching the ice VI position a second time at 132.5 K. Such thermal behaviour could not be explained without phase changes, and without invoking an ice VI[‡] transition state in the order-order transition from ice XIX to ice XV. The disappearance of ice XIX can be best seen at 1.868 Å. This comparably intense feature disappears as ice XV and ice VI form. The feature can be seen at least up to 102.5 K, maybe even 105 K, above which ice XIX has fully disappeared in the diffraction experiment. This is fully consistent with the onset temperature of 107±1 K obtained in the calorimetry experiment in Figure 1C, where the onset in the fast heating scans marks the full conversion in the slow heating experiment. The disappearance of the ice XIX features at 2.01, 2.05, 2.25 and 2.33 Å is fully consistent with this. Figure 4 shows the changes in c-axis upon transforming ice XIX to ice XV. It is immediately evident that ice XIX features a shorter length than ice VI, whereas ice XV shows a longer one. This explains why high pressure favors the formation of ice XIX over ice XV and *vice versa* at low pressure. At about 107 K the c-axis length obtained in the heating scan of ice XIX crosses the c-axis length of undoped ice VI. This is exactly where the disordered transition state ice VI[‡] is indicated in the calorimetry and neutron diffraction experiments described above. Above 130 K the c-axis length in ice XV then drops back from 5.805 to 5.792 Å, i.e., the value of ice VI. Thus, the transition sequence ice XIX→ice VI[‡]→ice XV→ice VI is clearly evidenced from these heating experiments and marked accordingly in Figure 1A using the coloured boxes.

Figure 4: Change in *c*-axis length upon heating ice XIX (red squares and green diamonds, obtained from Rietveld refinement of the data set shown in Figure 3) compared with a heating scan of undoped ice VI (circles).



Refinement of ice XIX from neutron powder data

The data for pure ice VI were refined by the Rietveld method in GSAS/ExpGui^{32,33}, starting from the structural model of Kuhs *et al.*³⁰. This yielded a fit with $\chi^2 = 2.307$ and weighted Rietveld powder statistic $wRp = 1.50\%$. Lattice parameters for ice VI at 70 K were found to be $a = 6.242485(11)$ Å, $c = 5.770048(22)$ Å, $V = 224.851(1)$ Å³. This structure refinement formed the basis for deriving models to test against the ice XIX data. One observes in the doped ice sample that many peaks permitted by the $P4_2/nmc$ space-group of ice VI, but which have negligible or zero intensity in ice VI, adopt a measurable intensity in ice XIX, albeit being very broad. Examples include the 212 and 311 peaks at $d = 2.00$ and 1.868 Å respectively (marked * in Figure 5). In addition to this, there are a few exceptionally weak and broad peaks that are not permitted by the cell metric of ice VI, which can only be accounted for by the development of a supercell. Most notable are the super-lattice peaks at 2.326 and 2.254 Å, respectively (marked † in Figure 5). Indexing of the ice XIX powder diffraction data, including the weak super-lattice Bragg peaks was done using DICVOL06³⁴, from which a $\sqrt{2} \times \sqrt{2} \times 1$ super-cell with twice the unit-cell volume of ice VI is obtained. Despite the high resolution of HRPD the broad peaks characteristic of ice XIX preclude unambiguous detection of any evidence for orthorhombic or monoclinic distortions of the super-cell by the splitting of Bragg peaks or even the development of noticeable shoulders. Whole-pattern profile fitting using the LeBail method inevitably results in better fits to the data with lower symmetry cell metrics, simply by virtue of the extra degrees of freedom, when the same result might equally be achieved with a higher symmetry cell and a more complex description of the peak shapes. On this basis, possible distortions of the unit-cell to lower symmetry monoclinic or triclinic cells were precluded from further consideration.

In total almost 2000 possible structure models are feasible for the supercell of double the ice VI unit cell³⁵. This overwhelming number of possible structures could be narrowed down by investigating each of the possible subgroups of the $\sqrt{2} \times \sqrt{2} \times 1$ super-cell regarding its compatibility with the ice VI-oxygen sublattice and Bernal-Fowler rules. After analysis through the subgroup tool in BILBAO³⁶⁻³⁸, ruling out lower symmetry monoclinic and triclinic space-groups as well as centred space-groups (by virtue of the observed reflection conditions), a set of 21 higher symmetry space groups is obtained – $P\bar{4}$, $P4_2$, $P\bar{4}2_1m$, $P\bar{4}2m$, $P4_2nm$, $P4_2cm$, $Pbcn$, $Pcca$, $Pnna$, $Pban$, $Pnn2$, $Pna2_1$, $Pba2$, $Pnc2$, $Pca2$, $Pcc2$, $P2_12_12$, $P222_1$, $P222$, $Pmmn$ and $Pmm2$. In order to investigate their compatibility with the O-lattice, the structure was centred in line with their respective transformation matrix³⁶⁻³⁸. This procedure is illustrated in the Supporting Information and filters out all space groups, except for five: $P\bar{4}$, $P4_2$, $P2_12_12$, $Pcc2$ and $Pcca$. In order to obtain a feasible set of candidate structures, the H-atom networks of these space groups have to be taken into account. That can be done by observing both Bernal-Fowler rules and the respective space-group symmetry. Specifically, each H-site is reflected through all symmetry operations so that H-positions of the same occupancy could be found. The occupancies of even more positions were derived from the Bernal-Fowler rules, as illustrated in Supporting-Figure 3 on the example of space group $Pcc2$, which implies that a structural model in space-group $Pcc2$ is necessarily only partially ordered. In total 109 valid structures in five space groups could be determined as possible candidate structure through these considerations, which can still not be tested quantitatively against the data. Moreover, the deviation of these structures from the average ice VI structure is very small and the amount of information required to describe this is represented by just a few quite weak fundamental and super-lattice peaks. Hence, the refinement of structural models is quite delicate, requiring restraints, constraints and damping in order to avoid divergence and to arrive at stable solutions. Even then, the difference in the statistical quality of the fit between models turns out to be small. We have, therefore, based our choice of tested structures on a few specific examples, and once we became aware of the structure fitting reported by Yamane *et al.* on ArXiv³⁹ we have chosen to report the equivalent best-fitting models in space groups $P\bar{4}$ and $Pcc2$.

The former turns out to be the best fit to the neutron powder diffraction data also in our case. Hence their data obtained *in situ* at 1.6 GPa and our data obtained *ex situ* at ~50 mbar can be described using the same structural models and we conclude that their work and ours indicates the same partially ordered superstructure, described as ice XIX. The quality of the fits to the diffraction data are shown in Figures 5 (for $P\bar{4}$) and Supporting-Figure 4 (for $Pcc2$). These refinements yield accurate atomic coordinates, D-atom occupancies and average isotropic displacement parameters, being reported in Table 1 (for $P\bar{4}$) and Supporting-Table 1 (for $Pcc2$), using the atom labelling as shown in Figure 6 and Supporting Figure 5, respectively. The two models differ from each other in one important aspect: the two interpenetrating frameworks in the $P\bar{4}$ model are not related by symmetry and we observe that one of the two frameworks becomes substantially more ordered than the other (where site-symmetry constraints limit the occupancy of many H-atoms sites to remain = 0.5). On the other hand, the two frameworks in the $Pcc2$ model are related by symmetry and thus the degree of order achieved is the same in both components of the framework.

Our best structural model is the tetragonal $P\bar{4}$ model, with the $Pcc2$ model being nearly statistically indistinguishable, so that a clear distinction is not possible based on the observed broad peaks. For the tetragonal $P\bar{4}$ model a χ^2 of 3.278 was obtained, with $wRp = 2.38\%$. The tetragonal lattice parameters at 70 K are $a = 8.834721(33)\text{ \AA}$, $c = 5.75542(5)\text{ \AA}$, $V = 449.224(4)\text{ \AA}^3$. With respect to an exact $\sqrt{2} \times \sqrt{2} \times 1$ super-cell of ice VI, the volume of ice XIX is smaller by $\Delta V/V = -0.11\%$. This reduction in volume is dominated by a shortening of the c -axis (-0.254%) partially offset by a small expansion in the two orthogonal directions perpendicular to c . For the orthorhombic $Pcc2$ model (see Supporting Information), a χ^2 of 4.018 was obtained, with $wRp = 2.63\%$. The orthorhombic lattice parameters at 70 K are $a = 8.84253(7)\text{ \AA}$, $b = 8.82654(7)\text{ \AA}$, $c = 5.75559(5)\text{ \AA}$, $V = 449.218(5)\text{ \AA}^3$. In common with the tetragonal model, we observe a reduction in volume relative to ice VI of approximately -0.10% , much of which is due to contraction of the c -axis. That is, c -axis contraction is necessary to reach ice XIX from ice VI, which can be achieved under high-pressure conditions near 2 GPa, but not at low-pressure conditions. In a very similar manner to the ordering transition of ice VI to yield ice XIX, preferential contraction of the c -axis of ice I_h is observed upon transformation to the ferroelectrically-ordered phase ice XI⁴⁰, and indeed on what is inferred to be local partial ordering of ice I_h on cooling towards the ordering transition⁴¹.

Figure 5: Neutron powder diffraction data for ice XIX (red circular symbols) and the fit calculated from the refined $P\bar{4}$ model (green line), with the background subtracted. The difference between the model and data is represented by the purple line underneath the diffraction pattern, and the positions of the Bragg peaks are indicated by vertical black tick marks. The inset shows the region between 1.7 and 2.45 Å d-spacing where peaks appear that are permitted by the ice VI cell metric but have little or no intensity in ice VI (*) and where super-lattice peaks are observed (†).

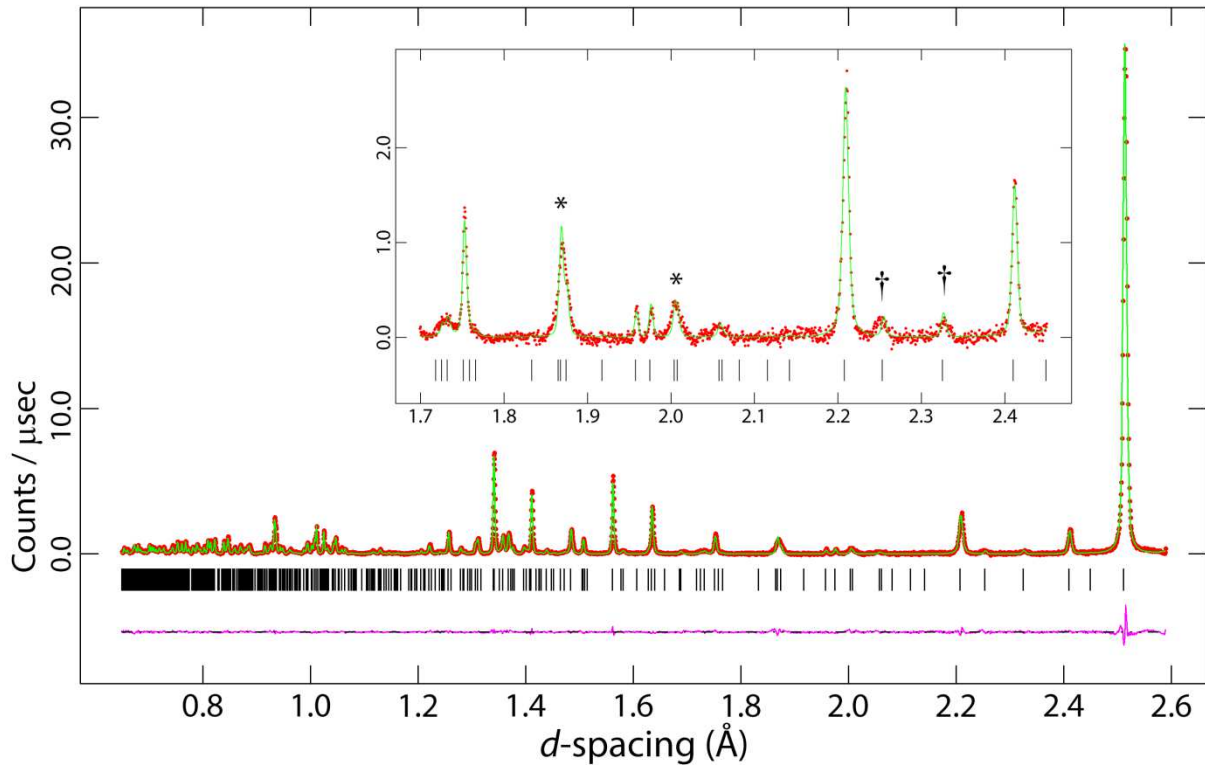


Figure 6: Unit-cell of ice XIX (refined $P\bar{4}$ model) viewed along the c -axis, showing the atom labelling scheme used in Table 1. Shading of the hydrogen atoms indicates the occupancy, reported quantitatively in Table 1.

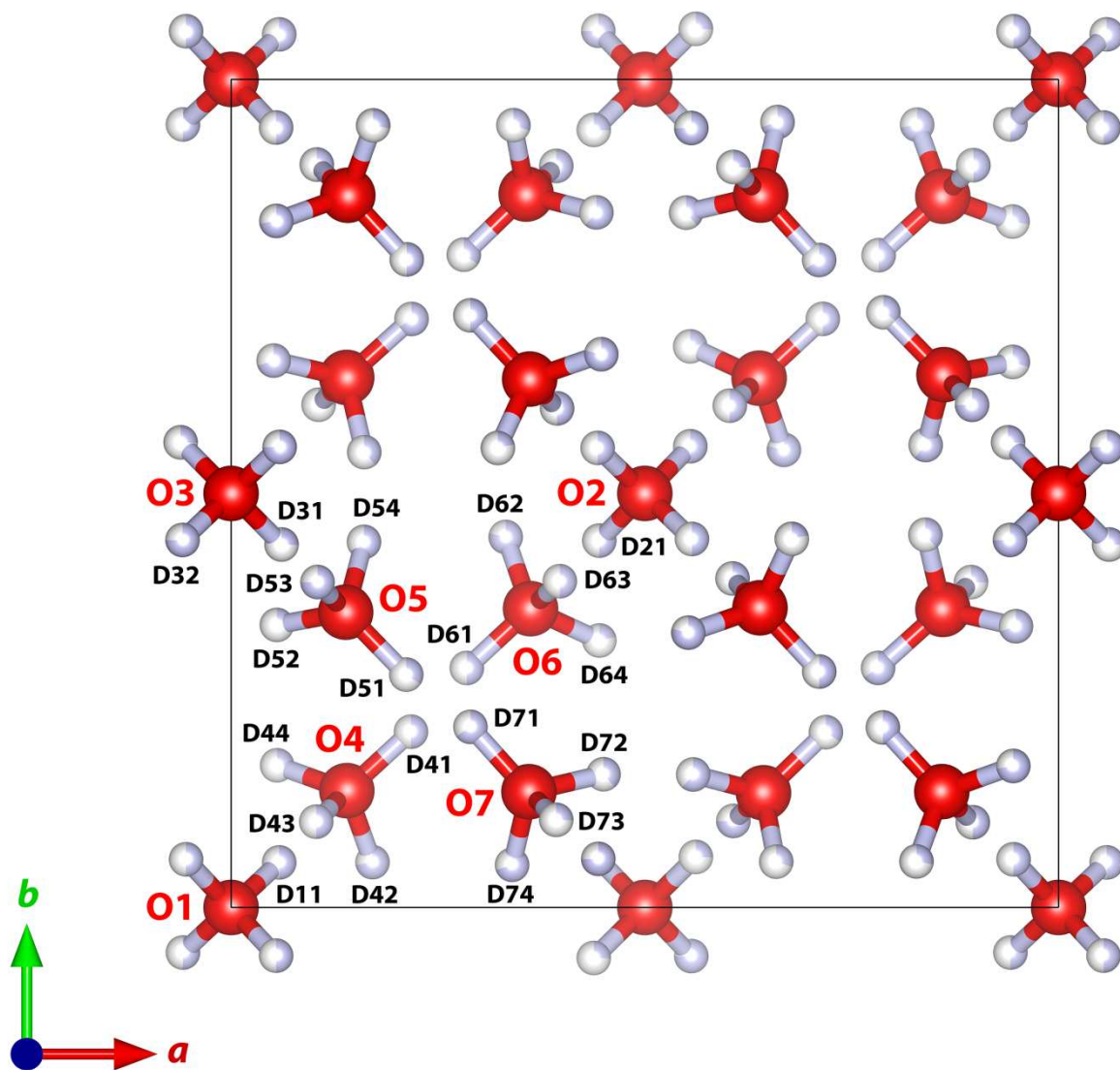


Table 1: Refined structure using the $P\bar{4}$ model

$a = b = 8.834721 (33) \text{ \AA}$

$c = 5.75542(5) \text{ \AA}$

$V = 449.224(4) \text{ \AA}^3$

Atom	Wyckoff position	x	y	z	Occ.	U_{iso}
O1	1 <i>b</i>	0.0	0.0	0.5	1.0	0.0081
O2	1 <i>d</i>	0.5	0.5	0.5	1.0	0.0081
O3	2 <i>g</i>	0.0	0.5	-0.0023(5)	1.0	0.0081
O4	4 <i>h</i>	0.1399(3)	0.1411(3)	0.1295(5)	1.0	0.0081
O5	4 <i>h</i>	0.1386(3)	0.3566(3)	0.6114(4)	1.0	0.0081
O6	4 <i>h</i>	0.3619(3)	0.3608(3)	0.1239(5)	1.0	0.0081
O7	4 <i>h</i>	0.3599(3)	0.1398(3)	0.6233(4)	1.0	0.0081
D11	4 <i>h</i>	0.0582(3)	0.0544(4)	0.3957(2)	0.5	0.0238
D21	4 <i>h</i>	0.4450(4)	0.4430(4)	0.3950(2)	0.5	0.0238
D31	4 <i>h</i>	0.0610(5)	0.4383(5)	0.9079(8)	0.253(2)	0.0238
D32	4 <i>h</i>	-0.0587(5)	0.4438(5)	0.0989(5)	0.747(2)	0.0238
D41	4 <i>h</i>	0.2174(5)	0.2123(5)	0.1348(2)	0.5	0.0238
D42	4 <i>h</i>	0.1709(8)	0.0547(4)	0.0509(9)	0.723(8)	0.0238
D43	4 <i>h</i>	0.1029(9)	0.1036(9)	0.2683(7)	0.343(4)	0.0238
D44	4 <i>h</i>	0.0556(5)	0.1717(13)	0.0461(12)	0.277(8)	0.0238
D51	4 <i>h</i>	0.2117(6)	0.2812(6)	0.6143(23)	0.343(4)	0.0238
D52	4 <i>h</i>	0.0553(5)	0.3412(18)	0.5161(10)	0.299(4)	0.0238
D53	4 <i>h</i>	0.1045(8)	0.3930(7)	0.7530(6)	0.747(2)	0.0238
D54	4 <i>h</i>	0.1606(10)	0.4415(4)	0.5223(8)	0.614(3)	0.0238
D61	4 <i>h</i>	0.2849(5)	0.2892(5)	0.1324(23)	0.5	0.0238
D62	4 <i>h</i>	0.3319(8)	0.4474(4)	0.0446(9)	0.785(7)	0.0238
D63	4 <i>h</i>	0.3973(9)	0.3940(10)	0.2664(7)	0.5	0.0238
D64	4 <i>h</i>	0.4451(6)	0.3224(11)	0.0460(14)	0.217(7)	0.0238
D71	4 <i>h</i>	0.2893(5)	0.2181(5)	0.6206(14)	0.657(4)	0.0238
D72	4 <i>h</i>	0.4501(5)	0.1609(14)	0.5474(12)	0.386(3)	0.0238
D73	4 <i>h</i>	0.3929(13)	0.1058(13)	0.7666(7)	0.253(2)	0.0238
D74	4 <i>h</i>	0.3396(10)	0.0515(4)	0.5414(9)	0.701(4)	0.0238

Conclusions

We here report a novel ice structure and provide two possible crystal structures for it. Based on common practice, the availability of the crystal structure allows us to assign a Roman numeral to this ice phase. Following the latest discovery of the superionic phase ice XVIII appearing at ultrahigh-pressure, we here add ice XIX to the ice phase diagram in the versatile intermediate pressure range between 0.5 and 2.0 GPa, in which 13 ice polymorphs are now known. Ice XIX represents an ordered phase sharing the same oxygen atom topology with its parent, disordered ice VI, and its sibling, antiferroelectrically ordered ice XV. The tetragonal $P\bar{4}$ structure refines slightly better than the orthorhombic $Pcc2$ model. However, a clear distinction between the two structural models cannot be

made because of the broad peaks indicating the new structure. This is likely to be related to small domains of ice XIX. Indeed, with powder data alone, a conclusive determination of the symmetry resulting from the partial ordering is extremely difficult and efforts to prepare ice XIX as a single crystal are required, as well as systematic computational studies of the thousands of possible orientational configurations. The space group symmetry requires ice VI to be fully hydrogen disordered. Any change in hydrogen order has to be associated with breaking of the space group symmetry¹⁹. That is, fractional occupancies of D-atoms deviating from it make the case for a new ice structure, as is the case for both structures fitting the data. Both structures feature cancellation of dipole moments, such that the structure's partial hydrogen ordering is antiferroelectric. That is, our earlier speculation of a possible ferroelectric structure is incorrect^{23,24}. Also earlier theoretical predictions about a ferroelectric structure in the *Cc* space group are incorrect^{42,43}. While Nanda and Beran had correctly predicted that the *Cc* structure is less favourable than the experimental ice XV structure, the supercell necessary to describe ice XIX was not considered⁴⁴. We can certainly rule out any 1 x 1 x 1 unit cell, including the one for space-group *Cc*, e.g., because our sharp peak at 1.960 Å and the broad peak at about 2.01 Å would be absent in *Cc*. Knight and Singer examined $\sqrt{2} \times \sqrt{2} \times 2$ cells and found a nearly energetically degenerate antiferroelectric structure in *P2₁2₁2₁*⁴². Even though we do not see any evidence for a doubling along *c* in our ice XIX data, this illustrates how sensitive the ordering is to long-range interactions. And this is where more recent developments in DFT, such as the widespread and easy implementation of dispersion corrections, looks to be essential to solving this very delicate problem. Now that we have established the correct unit cell, it should be possible computationally to provide a robust prediction of the ground-state configuration in future work.

Upon heating ice XIX transforms in two steps first to ice XV above 107±1 K, and then to ice VI at 128 K. This is consistently seen in the heating scans in calorimetry (at 10 K/min) and neutron powder diffraction scans at HRPD (averaged over the whole run at 2.5 K/hour). This makes the case for the first order-order transition in the H-subnetwork in a given O-network in ice physics. Ice XIX shows an O-lattice and a partly ordered H-network, making the case for a fully crystalline polymorph, as opposed to a crystal that shows a disordered H-subnetwork. That is, ice XIX, formerly called ice β-XV, cannot be described as a deep glassy state. The mechanism of the order-order transition from ice XIX to ice XV is shown to proceed in an activated fashion, where the activation barrier needs to be determined in future work. In the present work we are able to show that a transient, disordered state is encountered as the transition state – called ice VI[‡]. The deep glassy state put forward in earlier work by Rosu-Finsen & Salzmann^{26,27} could then be the transiently encountered ice VI[‡], but not ice XIX. Yamane et al. suggest in their work that “it is necessary to investigate whether the decompressed samples retain the crystal structure of ice XIX as well as its crystallinity” and speculate about a transition from ice XIX to a deep glassy state upon decompression³⁹. The fact that the same structural models for ice XIX fit both their data recorded at 1.6 GPa (reported in ref. 39) and our data recorded at 50 mbar (reported in the present work) rules out the possibility of ice XIX turning into deep glassy ice upon pressure change. The decompression-induced transition from ice XIX to ice XV as suggested by Yamane et al.³⁹ is not observed in our work upon decompressing from 1.8 GPa at 70 K. A comparison of unit cell volumes at 1.6 GPa and 50 mbar translates into an approximate estimate for ice XIX's bulk modulus of 21 GPa at 70 K. This compares with a bulk modulus of 18.5 GPa for its disordered parent ice VI⁴⁵ and for ice I_h of 11.2 GPa⁷, both at 70 K.

Ice XIX represents the thermodynamically stable phase of water between 1.0 and 1.5 GPa, and below 103 K, as argued by us earlier²³. That is, ice XIX occupies a substantial fraction of the intermediate pressure regime as a stable phase in water's *p-T* phase diagram. Taking the present results together

with the collected work by Salzmann et al. and ourselves on ice XV, it is evident that ice XV forms preferentially at low pressures below 1.0 GPa upon cooling ice VI, whereas for ice XIX high pressures exceeding 1.0 GPa are necessary. At 1 bar ice XV forms, but not ice XIX. At 2.0 GPa ice XIX forms, but not ice XV. At intermediate pressures there is competition between both, where pressure determines the kinetics and the fractions of ice XV and XIX. This is due to the compressed c-axis in ice XIX and the elongated c-axis in ice XV, both compared to the parental ice VI.

Methods

Sample Preparation

Sample preparation was done using the same set of equipment as used in our previous work²³. Ice XIX samples were prepared by (i) cooling 600 μ l 0.01 M DCl in D₂O:H₂O mixtures (0.04 to 99.99% H₂O) to 77 K, (ii) compressing to 1.8 GPa using a piston-cylinder setup with an 8 mm diameter bore in a Zwick BZ100 material testing machine, (iii) heating to 255 K, followed by (iv) slow cooling at rates of 0.1 to 3.0 K/min to 77 K. Undoped ice VI was prepared following a similar pathway using a 95:5 D₂O:H₂O mixture. After cooling to 77 K ice VI samples were compressed to 1.0 GPa before heating to 255 K, followed by quenching with liquid nitrogen at \approx 80 K/min. After releasing the pressure at 77 K, ice XIX and ice VI samples were recovered and stored under liquid nitrogen at atmospheric pressure. The ice XV reference was prepared *in situ* from ice XIX by heating to 135 K at 50 mbar (converting it to ice VI) and then recooling it with 0.4 K/min to 80 K (converting it to ice XV).

Differential-Scanning Calorimetry

All quench-recovered ices were analyzed calorimetrically using a Perkin Elmer DSC 8000 at ambient pressure. The samples were encapsulated in aluminum crucibles under liquid nitrogen and transferred to the precooled oven of the calorimeter. Every batch was characterized by heating at 10 K/min from 93 to 253 K, which leads to the transformation of both, ice XIX (over the sequence ice VI[†] \rightarrow XV \rightarrow VI) and ice VI, to ice I_h. The resulting ice I_h was cooled to 93 K and heated in a second scan to 313 K. The second scan was used to correct the background of the first heating run. The enthalpies of fusion of H₂O⁴⁶ and D₂O⁴⁷, 6012 and 6280 J/mol, were used to determine the mass of ice inside the crucible. The baseline was interpolated between the straight sections before the first and after the second endotherm to evaluate peak areas, onset and offset points. In selected experiments, ice XIX (D₂O:H₂O = 95:5) samples were heated from 93 to 120 K at 10 K/min and annealed at this temperature for 30 min to allow ice VI[†] to transform to ice XV. Afterwards, the samples were heated to 253 K to record the second endotherm pertaining to the ice XV to ice VI transition.

Neutron powder diffraction

Samples of pure D₂O ice VI and doped ice XIX were examined using neutron powder diffraction methods on the High Resolution Powder Diffractometer (HRPD) at the ISIS Neutron and Muon Spallation Source, Rutherford Appleton Laboratory, U. K.⁴⁸. The various ices were measured in slab-geometry sample holders that are described in detail elsewhere⁴⁹, having internal dimensions with width, height and depth = 18 x 23 x 5 mm relative to the incident neutron beam. These were partially assembled and immersed in liquid nitrogen for the loading procedure. The powdered samples were transferred from a nitrogen-chilled steel cryomortar into the sample holder using a nitrogen-chilled spoon. Once filled, the ‘back’ vanadium foil window of the sample can was attached with screws. Both the ‘front’ (i.e., beam-facing) and ‘back’ windows were sealed with 1 mm indium wire to prevent leakage of material from the interior. The front windows and the body of the sample holder were masked with Gd and Cd foil.

The fully-assembled sample holder was then transferred into a top-loading Closed Cycle Refrigerator (CCR) mounted on the HRPD beam line at 70 K. Temperature control was achieved using a cartridge heater and a RhFe thermometer inserted into the aluminium frame of the sample holder, the background temperature of the He exchange gas being maintained \sim 30 K below the sample temperature where possible. Moving from one temperature to another was done at a rate of 3 K min⁻¹ with a mandatory wait of 10 minutes at each temperature prior to beginning a measurement in order to be sure that complete thermal equilibrium of the sample was achieved.

Data were collected using a neutron time-of-flight window extending from 30 to 130 ms. In HRPD's highest resolution backscattering detector banks, this TOF range yields data covering d-spacings from 0.65 to 2.60 Å, which contains the great majority of Bragg reflections required for a high-precision structure refinement. For example, ice VI has >240 reflections in this d-spacing range whereas the next available detector bank at $2\theta = 90 \pm 10^\circ$, which allows us to access d-spacings from 1–4 Å, contains only an additional five reflections. Nevertheless, these fewer but more intense peaks are often useful for rapid tracking of phase changes, as shown in Figure 2.

Raw time-of-flight data were focussed to a common scattering angle for each detector bank, normalised to the incident spectrum and corrected for instrument efficiency by reference to measurements of a V:Nb rod and the empty instrument with the Mantid suite of powder diffraction algorithms^{50,51}. The CCR makes a comparatively small contribution to the background, but of most concern in the case of these data are the weak peaks from the vanadium foil windows used on the CCR tails, as they occur in a region of very weak peaks of interest from the ice XIX sample. Consequently, a long background measurement from an empty masked slab can in the CCR was made at 70 K to ensure accurate subtraction of the parasitic peaks from the structural datasets obtained from ice VI and ice XIX at 70 K.

Structural models in space groups $P\bar{4}$ and $Pcc2$ were fitted to the high-resolution neutron powder diffraction data using the Rietveld method implemented in GSAS/ExpGui. Bond length restraints of 0.925 ± 0.015 Å were placed on the O–D bond length, based on the average length found in our ice VI refinements; no bond angle restraints were imposed. Constraints were applied to the isotropic displacement parameters, U_{iso} , to achieve an average value for each type of atom (O or D). Constraints were also used to ensure that the D-atom occupancy along each D-bonded O–O vector summed to one. Chemical restraints were imposed to insure that, where not otherwise determined by the occupancy constraints or by symmetry, the total number of D-atoms per O-atom remained fixed equal to two.

Acknowledgements

The authors thank the STFC ISIS facility for a beam time allocation, proposal RB2000132 (doi:10.5286/ISIS.E.RB2000132), and the provision of technical resources with which to carry out this work. We gratefully acknowledge support by the Austrian Science Fund (FWF) under grant number I1392.

References

- 1 Bernal, J. D. & Fowler, R. H. A theory of water and ionic solutions, with particular reference to hydrogen and hydroxyl ions. *J. Chem. Phys.* **1**, 515-548, doi:10.1063/1.1749327 (1933).
- 2 Pauling, L. The structure and entropy of ice and of other crystals with some randomness of atomic arrangement. *J. Am. Chem. Soc.* **57**, 2680-2684 (1935).
- 3 Kawada, S. Dielectric Dispersion and Phase-Transition of KOH Doped Ice *J. Phys. Soc. Japan* **32**, 1442, doi:10.1143/jpsj.32.1442 (1972).
- 4 Tajima, Y., Matsuo, T. & Suga, H. Calorimetric study of phase transition in hexagonal ice doped with alkali hydroxides. *J. Phys. Chem. Solids* **45**, 1135-1144 (1984).
- 5 Oguro, M. & Whitworth, R. W. Dielectric observation of the transformation of single crystals of KOH-doped ice Ih to ice XI. *J. Phys. Chem. Solids* **52**, 401-403, doi:10.1016/0022-3697(91)90090-m (1991).
- 6 Jackson, S. M., Nield, V. M., Whitworth, R. W., Oguro, M. & Wilson, C. C. Single-crystal neutron diffraction studies of the structure of ice XI. *J. Phys. Chem. B* **101**, 6142-6145, doi:10.1021/jp9632551 (1997).
- 7 Petrenko, V. F. & Whitworth, R. W. *Physics of Ice*. (Oxford University Press, 1999).
- 8 Koster, K. W. *et al.* Doping-enhanced dipolar dynamics in ice V as a precursor of hydrogen ordering in ice XIII. *Phys. Rev. B* **94**, 184306, doi:10.1103/PhysRevB.94.184306 (2016).
- 9 Handa, Y. P., Klug, D. D. & Whalley, E. Energies of the phases of ice at low temperature and pressure relative to ice Ih. *Can. J. Chem.* **66**, 919-924 (1988).
- 10 Singer, S. J. *et al.* Hydrogen-bond topology and the ice VII/VIII and ice Ih/XI proton-ordering phase transitions. *Phys. Rev. Lett.* **94**, 135701, doi:10.1103/PhysRevLett.94.135701 (2005).
- 11 Parkkinen, P., Riikonen, S. & Halonen, L. Ice XI: Not That Ferroelectric. *J. Phys. Chem. C* **118**, 26264-26275, doi:10.1021/jp510009m (2014).
- 12 Salzmann, C. G., Radaelli, P. G., Hallbrucker, A., Mayer, E. & Finney, J. L. The Preparation and Structures of Hydrogen Ordered Phases of Ice. *Science* **311**, 1758-1761 (2006).
- 13 Salzmann, C. G., Hallbrucker, A., Finney, J. L. & Mayer, E. Raman spectroscopic study of hydrogen ordered ice XIII and of its reversible phase transition to disordered ice V. *Phys. Chem. Chem. Phys.* **8**, 3088-3093 (2006).
- 14 Salzmann, C. G., Radaelli, P. G., Hallbrucker, A., Mayer, E. & Finney, J. L. New hydrogen ordered phases of ice. *Physics and Chemistry of Ice, [Proceedings of the International Conference on the Physics and Chemistry of Ice], 11th, Bremerhaven, Germany, July 23-28, 2006*, 521-528 (2007).
- 15 Salzmann, C. G., Radaelli, P. G., Finney, J. L. & Mayer, E. A calorimetric study on the low temperature dynamics of doped ice V and its reversible phase transition to hydrogen ordered ice XIII. *Phys. Chem. Chem. Phys.* **10**, 6313-6324 (2008).
- 16 Salzmann, C. G., Hallbrucker, A., Finney, J. L. & Mayer, E. Raman spectroscopic features of hydrogen-ordering in ice XII. *Chem. Phys. Lett.* **429**, 469-473 (2006).
- 17 Koster, K. W. *et al.* Dynamics enhanced by HCl doping triggers full Pauling entropy release at the ice XII-XIV transition. *Nature Comm.* **6**, 7349, doi:10.1038/ncomms8349 (2015).
- 18 Fuentes-Landete, V., Koster, K. W., Bohmer, R. & Loerting, T. Thermodynamic and kinetic isotope effects on the order-disorder transition of ice XIV to ice XII. *Phys. Chem. Chem. Phys.* **20**, 21607-21616, doi:10.1039/c8cp03786h (2018).
- 19 Salzmann, C. G., Radaelli, P. G., Mayer, E. & Finney, J. L. Ice XV: A New Thermodynamically Stable Phase of Ice. *Phys. Rev. Lett.* **103**, 105701, doi:10.1103/PhysRevLett.103.105701 (2009).
- 20 Johari, G. P. & Whalley, E. Evidence for a very slow transformation in ice VI at low temperatures. *J. Chem. Phys.* **70**, 2094-2097 (1979).
- 21 Whale, T. F., Clark, S. J., Finney, J. L. & Salzmann, C. G. DFT-assisted interpretation of the Raman spectra of hydrogen-ordered ice XV. *J. Raman Spect.* **44**, 290-298, doi:10.1002/jrs.4170 (2013).

- 22 Salzmann, C. G. *et al.* Detailed crystallographic analysis of the ice VI to ice XV hydrogen
ordering phase transition. *J. Chem. Phys.* **145**, 204501, doi:10.1063/1.4967167 (2016).
- 23 Gasser, T. M. *et al.* Experiments indicating a second hydrogen ordered phase of ice VI. *Chem.
Sci.* **9**, 4224-4234, doi:10.1039/c8sc00135a (2018).
- 24 Thoeny, A. V., Gasser, T. M. & Loerting, T. Distinguishing ice beta-XV from deep glassy ice VI:
Raman spectroscopy. *Phys. Chem. Chem. Phys.* **21**, 15452-15462, doi:10.1039/c9cp02147g
(2019).
- 25 Shephard, J. J. & Salzmann, C. G. The complex kinetics of the ice VI to ice XV hydrogen
ordering phase transition. *Chem. Phys. Lett.* **637**, 63-66, doi:10.1016/j.cplett.2015.07.064
(2015).
- 26 Rosu-Finsen, A. & Salzmann, C. G. Origin of the low-temperature endotherm of acid-doped
ice VI: new hydrogen-ordered phase of ice or deep glassy states? *Chem. Sci.* **10**, 515-523,
doi:10.1039/c8sc03647k (2019).
- 27 Rosu-Finsen, A., Amon, A., Armstrong, J., Fernandez-Alonso, F. & Salzmann, C. G. Deep-Glassy
Ice VI Revealed with a Combination of Neutron Spectroscopy and Diffraction. *J. Phys. Chem.
Lett.* **11**, 1106-1111, doi:10.1021/acs.jpcllett.0c00125 (2020).
- 28 Millot, M. *et al.* Nanosecond X-ray diffraction of shock-compressed superionic water ice.
Nature **569**, 251-255, doi:10.1038/s41586-019-1114-6 (2019).
- 29 Fuentes-Landete, V., Plaga, L. J., Keppler, M., Bohmer, R. & Loerting, T. Nature of water's
second glass transition elucidated by doping and isotope substitution experiments. *Phys. Rev.
X* **9**, 011015, doi:10.1103/PhysRevX.9.011015 (2019).
- 30 Kuhs, W. F., Finney, J. L., Vettier, C. & Bliss, D. V. Structure and hydrogen ordering in ices VI,
VII, and VIII by neutron powder diffraction. *J. Chem. Phys.* **81**, 3612-3623 (1984).
- 31 Kamb, B. Structure of ice VI. *Science* **150**, 205-209 (1965).
- 32 Toby, B. H. EXPGUI, a graphical user interface for GSAS. *J. Appl. Crystallogr.* **34**, 210-213,
doi:10.1107/s0021889801002242 (2001).
- 33 General Structure Analysis System (GSAS) (Los Alamos National Laboratory Report LAUR 86-
748, Los Alamos, New Mexico, USA, 2000).
- 34 Louer, D. & Boulton, A. Powder pattern indexing and the dichotomy algorithm. *Z. Kristall.*, 191-
196 (2007).
- 35 Komatsu, K. *et al.* Partially ordered state of ice XV. *Sci. Rep.* **6**, 28920, doi:10.1038/srep28920
(2016).
- 36 Aroyo, M. I. *et al.* Crystallography online: Bilbao Crystallographic Server. *Bulg. Chem. Comm.*
43, 183-197 (2011).
- 37 Aroyo, M. I. *et al.* Bilbao crystallographic server: I. Databases and crystallographic computing
programs. *Z. Kristall.* **221**, 15-27, doi:10.1524/zkri.2006.221.1.15 (2006).
- 38 Aroyo, M. I., Kirov, A., Capillas, C., Perez-Mato, J. M. & Wondratschek, H. Bilbao
crystallographic server. II. Representations of crystallographic point groups and space groups.
Acta Cryst. **62A**, 115-128, doi:10.1107/s0108767305040286 (2006).
- 39 Yamane, R. *et al.* New diversity form of ice polymorphism: Discovery of second hydrogen
ordered phase of ice VI. <https://arxiv.org/abs/2006.10928v1> (2020).
- 40 Line, C. M. B. & Whitworth, R. W. A high resolution neutron powder diffraction study of D2O
ice XI. *J. Chem. Phys.* **104**, 10008-10013, doi:10.1063/1.471745 (1996).
- 41 Fortes, A. D. Structural manifestation of partial proton ordering and defect mobility in ice.
Phys. Chem. Chem. Phys. **21**, 8264-8274, doi:10.1039/c9cp01234f (2019).
- 42 Knight, C. & Singer, S. J. Prediction of a Phase Transition to a Hydrogen Bond Ordered Form
of Ice VI. *J. Phys. Chem. B* **109**, 21040-21046 (2005).
- 43 Kuo, J.-L. & Kuhs, W. F. A First Principles Study on the Structure of Ice-VI: Static Distortion,
Molecular Geometry, and Proton Ordering. *J. Phys. Chem. B* **110**, 3697-3703 (2006).
- 44 Nanda, K. D. & Beran, G. J. O. What Governs the Proton Ordering in Ice XV? *J. Phys. Chem.
Lett.* **4**, 3165-3169, doi:10.1021/jz401625w (2013).

- 45 Fortes, A. D., Wood, I. G., Tucker, M. G. & Marshall, W. G. The P-V-T equation of state of D2O ice VI determined by neutron powder diffraction in the range $0 < P < 2.6$ GPa and $120 < T < 330$ K, and the isothermal equation of state of D2O ice VII from 2 to 7 GPa at room temperature. *J. Appl. Cryst.* **45**, 523-534, doi:10.1107/s0021889812014847 (2012).
- 46 Hallbrucker, A. & Mayer, E. Calorimetric Study of the Vitrified Liquid Water to Cubic Ice Phase Transition. *J. Phys. Chem.* **91**, 503-505 (1987).
- 47 Long, E. A. & Kemp, J. D. The entropy of deuterium oxide and the third law of thermodynamics - Heat capacity of deuterium oxide from 15 to 298 degrees K - The melting point and heat of fusion. *J. Am. Chem. Soc.* **58**, 1829-1834, doi:10.1021/ja01301a001 (1936).
- 48 Ibberson, R. M. Design and performance of the new supermirror guide on HRPD at ISIS. *Nucl. Inst. & Meth. Phys. Res. A* **600**, 47-49, doi:10.1016/j.nima.2008.11.066 (2009).
- 49 Fortes, A. D. Accurate and precise lattice parameters of H2O and D2O ice Ih between 1.6 and 270 K from high-resolution time-of-flight neutron powder diffraction data. *Acta Cryst. B* **74**, 196-216, doi:10.1107/s2052520618002159 (2018).
- 50 Manipulation and Analysis Toolkit for Instrument Data; Mantid Project (2013).
- 51 Arnold, O. *et al.* Mantid-Data analysis and visualization package for neutron scattering and mu SR experiments. *Nucl. Inst. & Meth. Phys. Res. A* **764**, 156-166, doi:10.1016/j.nima.2014.07.029 (2014).

Supporting Information:

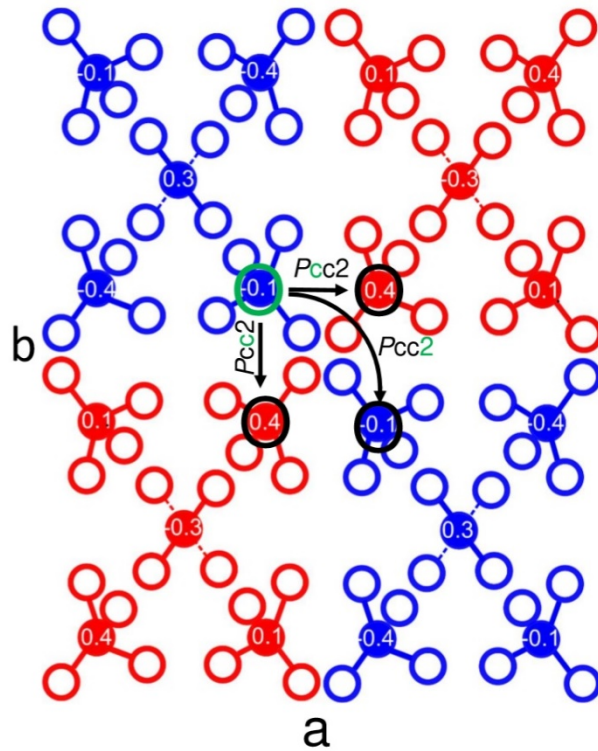
Calorimetric Analysis of the second endotherm (ice XV→ice VI)

Apparently, the second endotherm is much larger (48 J/mol) for the top two traces pertaining to H₂O ice β-XV, compared to all traces between 0.5 and 30% H₂O (7 J/mol), in which D₂O ice β-XV forms at 1.8 GPa. This prompts the question why the ice XV to ice VI transition is suppressed in D₂O ice β-XV samples. The answer is kinetics. In order to transform one ordered phase to another differently ordered phase an activation barrier needs to be overcome, where the transition state is necessarily disordered. We call this transition state ice VI[‡]. This transition state then needs to order again, and turn into ice XV. Ordering of ice VI[‡] is much faster for H₂O samples than for D₂O samples. The large kinetic isotope effect is evident from the width of the first endotherm, which increases from 12±1 K in protiated samples to 18±2 K in deuterated ones (see blue double-arrows in Figure 1C). In other words, the 2.5 minutes provided for the order in ice XV to develop inside the calorimetry instrument at a scanning rate of 10 K/min are not sufficient in deuterated samples, but in protiated ones. In order to make this point more evident we have conducted a calorimetry experiment, in which the heating scan was paused for 30 minutes at 120 K. In these 30 minutes there is ample time for D₂O ice XV to form, and upon commencing the heating scan a large second endotherm of 70 J/mol is also observed for D₂O samples (see dashed green line in Figure 1A at 5% H₂O). That is, 30 minutes at 120 K are enough for deuterated ice XV to fully develop from ice β-XV, but 2.5 minutes in the temperature interval 103-128 K are not. These calorimetric findings suggest that the transition sequence is a three-step process, as follows: In the first step ice β-XV transforms to ice VI[‡] at 103 K, causing the first endotherm. In the second step, between about 103 K and 128 K ice VI[‡] develops to the more stable ordered ice XV, where kinetics are the limitation. This sequence *via* ice VI[‡] describes how the first H-order-to-H-order transition in ice physics takes place. In the third step then ice XV disorders to produce metastable ice VI.

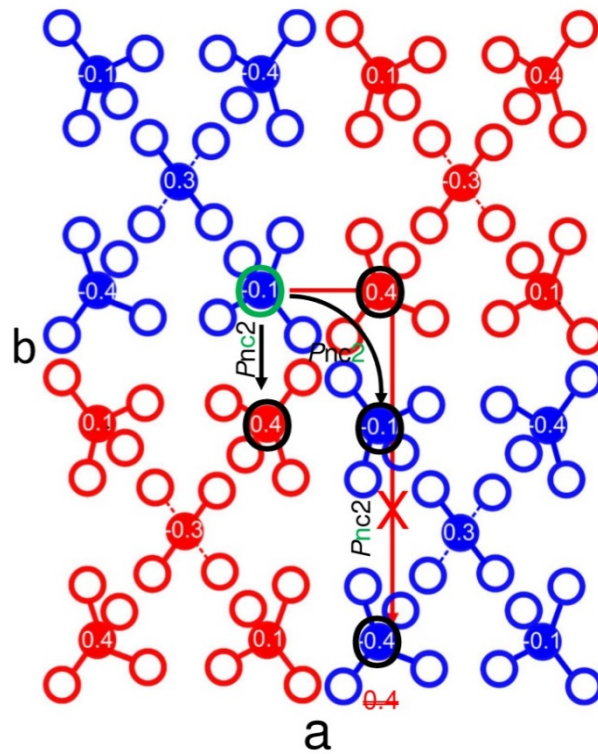
Ruling out space groups using Bilbao

In order to check for the validity of a given space group, the O-atoms were reflected through each symmetry element. Within valid space groups these reflections have to match exactly with positions of other O-atoms. This point is illustrated in Supp.-Figs. 1 and 2. In Supp.-Fig. 1, the O-atom circled in green was analysed for space group *Pcc2*. Its first reflected position can be obtained by reflection through the y-z-plane and a subsequent translation of half the lattice vector along z-direction (from -0.1 to 0.4). As we can find another O atom (circled in black) on that position, this symmetry operation is valid. Analogously, we can verify the reflection through the x-z-plane and the subsequent translation. Also, the twofold axis can be confirmed easily. In Supp.-Fig. 2, we can find a different situation. Here, space group *Pnc2* is considered and the O-atom circled in green has to be reflected through the y-z-plane and subsequently translated through half of the diagonal of the a-c-face. At that position, however, we cannot find an oxygen atom. That can easily be visualized by the z-positions as the greenly circled O-atom is, again, reflected from -0.1 to 0.4, whereas the oxygen atom at the respective position within the x-y-plane is set at z= -0.4.

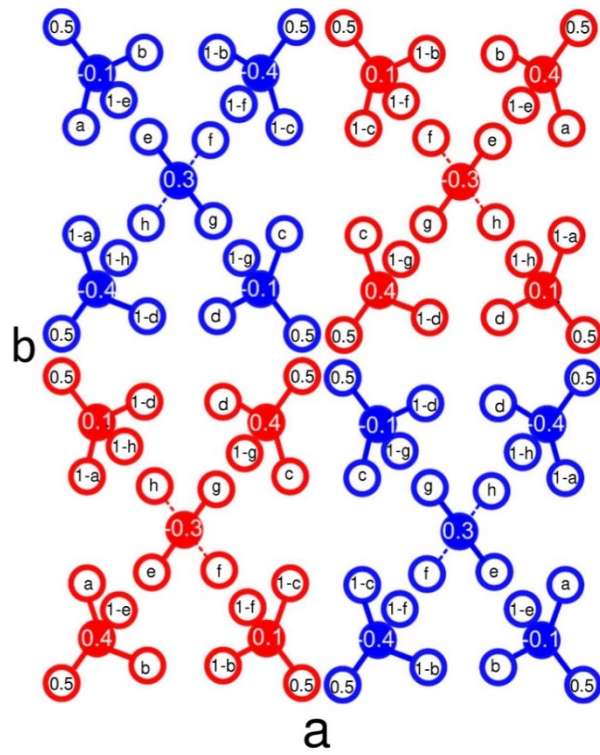
Supporting-Figure 1: $\sqrt{2} \times \sqrt{2} \times 1$ super-cell of the ice VI unit cell containing the reflection conditions of *Pcc2*: full circles represent O-atoms, empty circles H-sites, different colours different H-sublattices and white numbers the z-positions of the O-atoms.



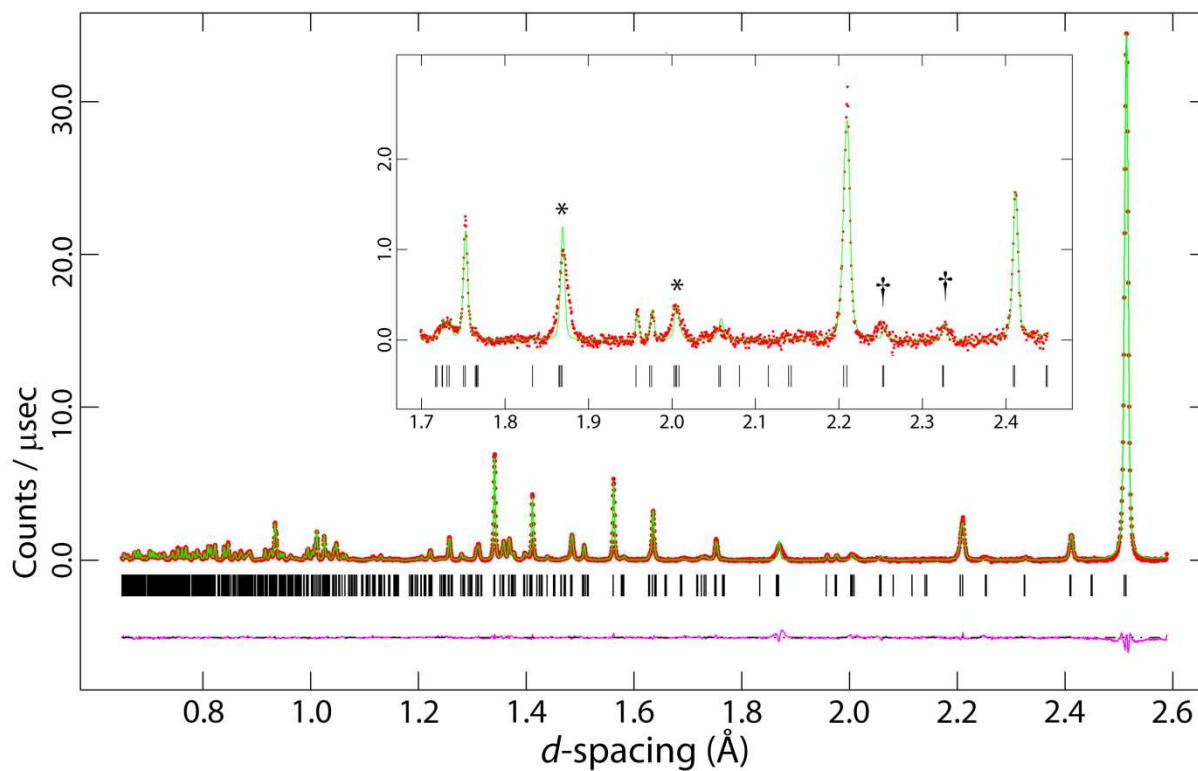
Supporting-Figure 2: $\sqrt{2} \times \sqrt{2} \times 1$ super-cell of the ice VI unit cell containing the reflection conditions of $Pnc2$: full circles represent O-atoms, empty circles H-sites, different colours different H-sublattices and white numbers the z-positions of the O-atoms.



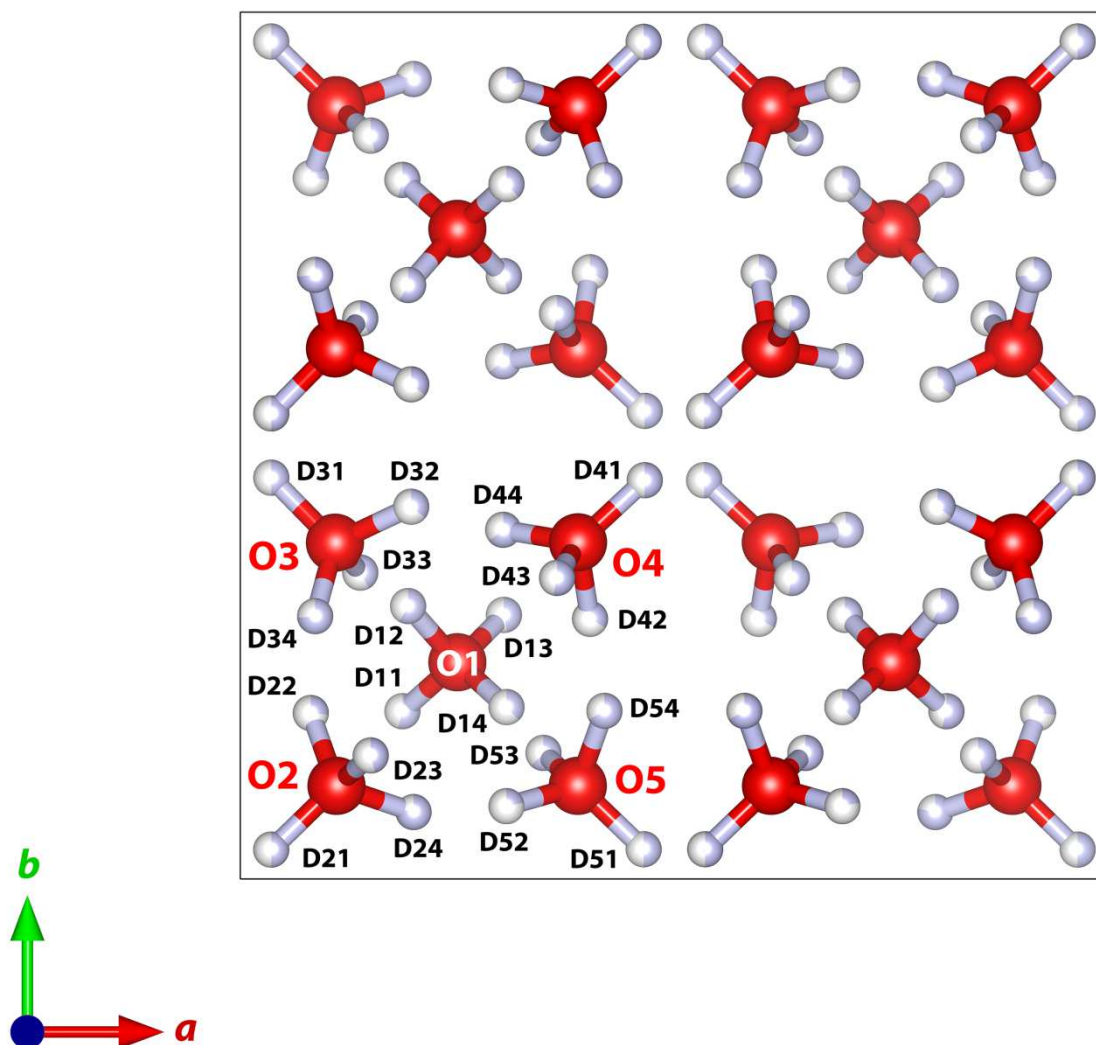
Supporting-Figure 3: Occupancies of the H-sites according to *Pcc2* symmetry operators.



Supporting-Figure 4: Neutron powder diffraction data for ice XIX (red circular symbols) and the fit calculated from the refined Pcc2 model (green line), with the background subtracted. The difference between the model and data is represented by the purple line underneath the diffraction pattern and the positions of the Bragg peaks are indicated by vertical black tick marks. The inset shows the region between 1.7 and 2.45 Å d-spacing where peaks appear that are permitted by the ice VI cell metric but have little or no intensity in ice VI (*) and where super-lattice peaks are observed (†).



Supporting-Figure 5: Unit-cell of ice XIX (refined Pcc2 model) viewed along the *c*-axis, showing the atom labelling scheme used in Supporting-Table 1.



Supporting-Table 1: Refined structure using the *Pcc2* model $a = 8.84253 (7) \text{ \AA}$ $b = 8.82654 (7) \text{ \AA}$ $c = 5.75559 (5) \text{ \AA}$ $V = 449.218 (5) \text{ \AA}^3$

Atom	Wyckoff position	<i>x</i>	<i>y</i>	<i>z</i>	Occ.	U_{iso}
O1	4 <i>e</i>	0.25	0.25	0.25	1.0	0.0081
O2	4 <i>e</i>	0.1107(2)	0.1074(2)	0.8770(3)	1.0	0.0081
O3	4 <i>e</i>	0.1092(2)	0.3881(2)	0.6322(3)	1.0	0.0081
O4	4 <i>e</i>	0.3892(2)	0.3884(2)	0.8695(3)	1.0	0.0081
O5	4 <i>e</i>	0.3888(2)	0.1073(2)	0.6259(3)	1.0	0.0081
D11	4 <i>e</i>	0.1869(4)	0.1933(5)	0.1555(6)	0.545(3)	0.0219
D12	4 <i>e</i>	0.1931(4)	0.3143(4)	0.3424(6)	0.579(2)	0.0219
D13	4 <i>e</i>	0.3036(5)	0.3046(5)	0.1400(6)	0.471(3)	0.0219
D14	4 <i>e</i>	0.3066(5)	0.1981(6)	0.3595(6)	0.383(3)	0.0219
D21	4 <i>e</i>	0.0356(4)	0.0340(4)	0.8910(14)	0.5	0.0219
D22	4 <i>e</i>	0.0814(10)	0.1914(4)	0.7917(9)	0.271(2)	0.0219
D23	4 <i>e</i>	0.1497(7)	0.1425(7)	0.0161(5)	0.455(3)	0.0219
D24	4 <i>e</i>	0.1994(3)	0.0774(6)	0.8042(7)	0.783(1)	0.0219
D31	4 <i>e</i>	0.0359(4)	0.4632(4)	0.6165(15)	0.5	0.0219
D32	4 <i>e</i>	0.1967(4)	0.4293(7)	0.6941(10)	0.357(3)	0.0219
D33	4 <i>e</i>	0.1389(8)	0.3537(8)	0.4875(5)	0.422(2)	0.0219
D34	4 <i>e</i>	0.0859(7)	0.3036(3)	0.7216(6)	0.729(2)	0.0219
D41	4 <i>e</i>	0.4660(4)	0.4601(4)	0.8609(13)	0.5	0.0219
D42	4 <i>e</i>	0.4042(12)	0.3005(4)	0.7845(8)	0.331(3)	0.0219
D43	4 <i>e</i>	0.3639(8)	0.3475(6)	0.0121(5)	0.529(3)	0.0219
D44	4 <i>e</i>	0.3032(3)	0.4039(8)	0.7798(6)	0.644(3)	0.0219
D51	4 <i>e</i>	0.4647(4)	0.0344(4)	0.6326(15)	0.5	0.0219
D52	4 <i>e</i>	0.3065(4)	0.0847(13)	0.7192(8)	0.217(1)	0.0219
D53	4 <i>e</i>	0.3496(6)	0.1451(6)	0.4887(5)	0.617(3)	0.0219
D54	4 <i>e</i>	0.4189(6)	0.1939(3)	0.7048(7)	0.669(3)	0.0219

Figures

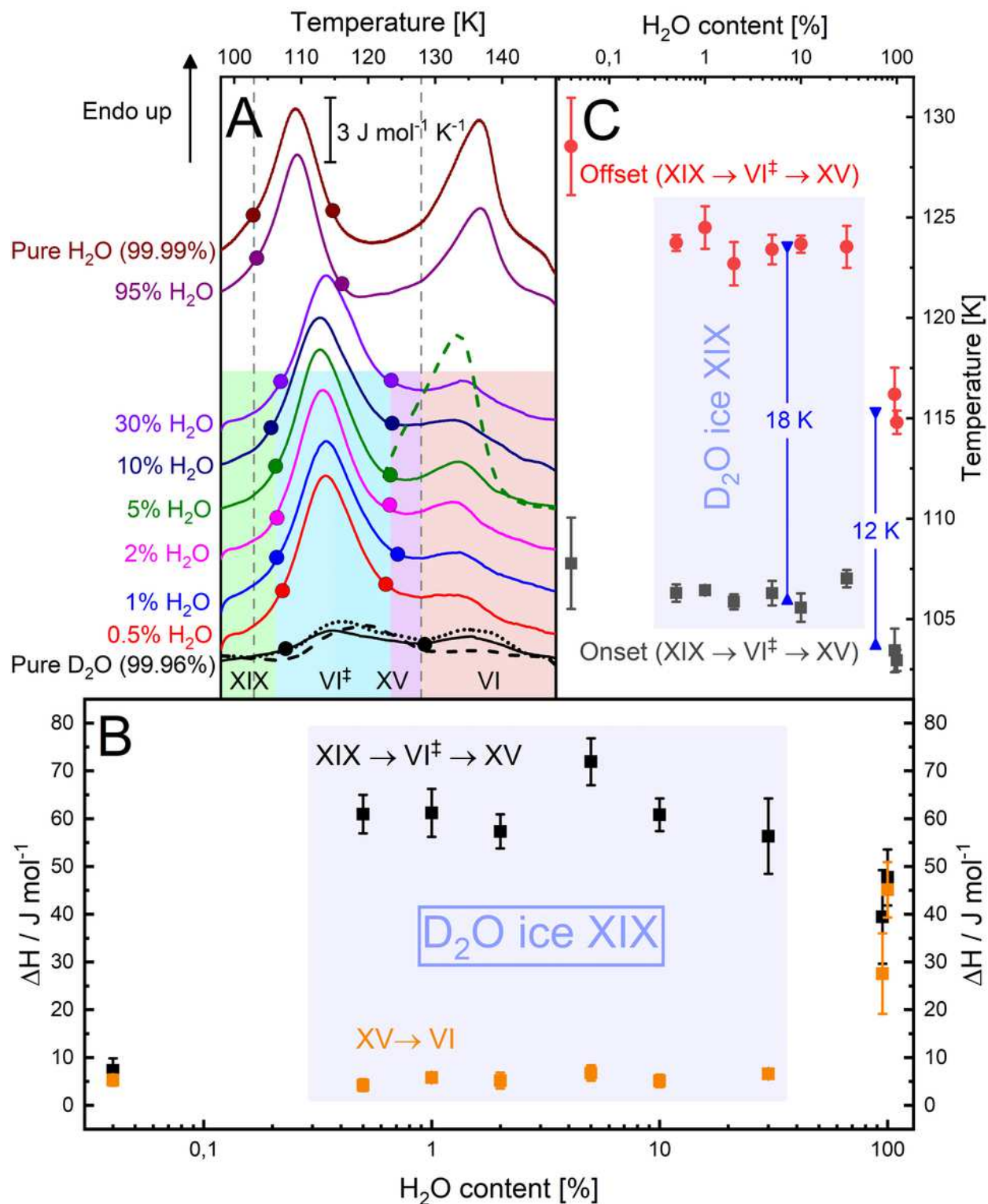


Figure 1

(A) Differential scanning calorimetry scans of ice XIX samples with different D₂O/H₂O ratios recorded at a heating rate of 10 K/min. The two endotherms indicate first the ice XIX → VI[‡] → XV and second the ice XV → VI transition. All full lines were recorded on samples slow-cooled at 1.8 GPa (see Methods). Dashed

lines mark heating scans of ice XIX annealed at 1.8 GPa and 106 K (black dashed line, pure D2O) and annealed at ambient pressure and 120 K (green dashed line, 5% H2O). Heating scan of ice XIX after very slow cooling at 1.8 GPa is shown as dotted black line (pure D2O). Onset and offset points for the first transition are marked by full circles. (B) Enthalpy changes associated with the two transitions (black squares: XIX \leftrightarrow VI \leftrightarrow XV; orange squares: XV \leftrightarrow VI). (C) Onset (black squares) and offset points (red circles). Error bars reflect both reproducibility and ambiguities in determining the points based on the tangent method. The width of the transition at 10 K/min is indicated through the blue double arrow.

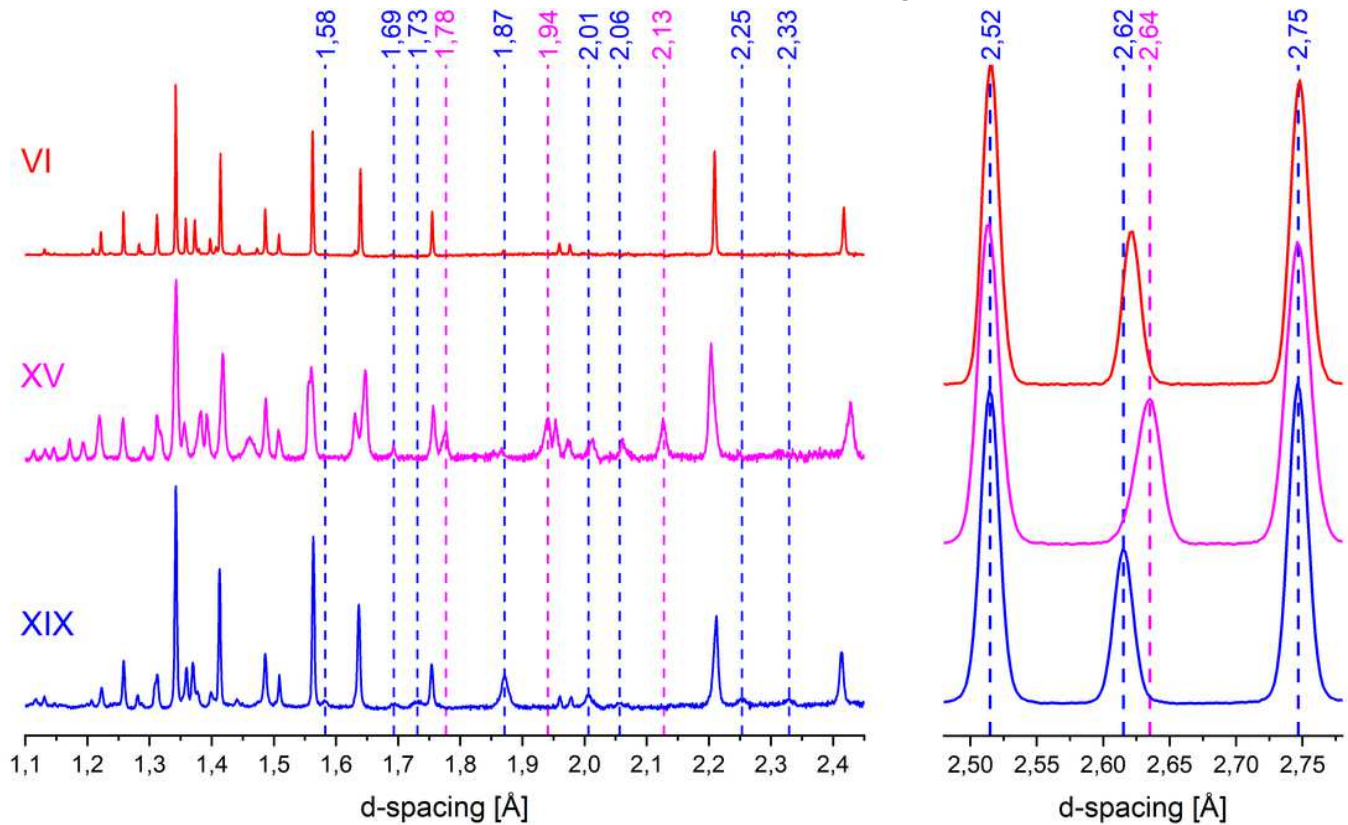


Figure 2

Comparison of ice XIX, ice XV and ice VI neutron powder diffraction patterns. Baselines were corrected with an 8 pt spline. Selected features of the ice XIX and ice XV diffractograms are highlighted by vertical, dashed blue and magenta lines, respectively. Note the sharp peaks in ice VI and the broader peaks in ices XV and XIX – this hints at particle size broadening from very small partially ordered domains. The diffractograms on the left were acquired in HRPD’s highest resolution backscattering banks ($2\theta = 165\pm 11^\circ$) whilst the three peaks shown on the right were recorded in the medium-resolution detectors at $2\theta = 90\pm 10^\circ$.

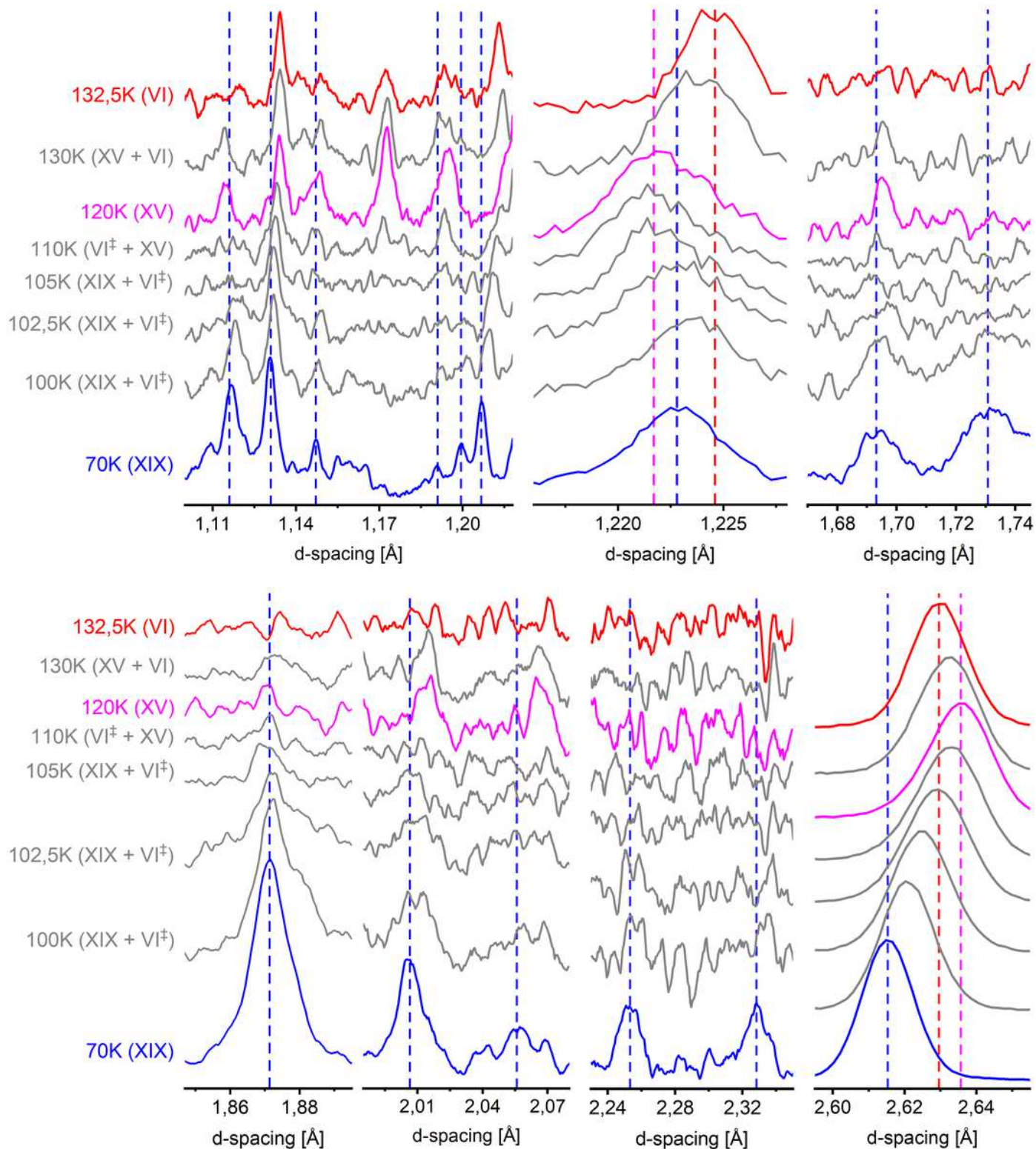


Figure 3

Heating of a D₂O ice XIX sample in HRPD, revealing transitions to ice XV (120K) (via ice VI[‡]) and to ice VI (132.5K). Data in Panel 1, 3, 4, 5 and 6 were smoothed using a 13pt Savitzky-Golay

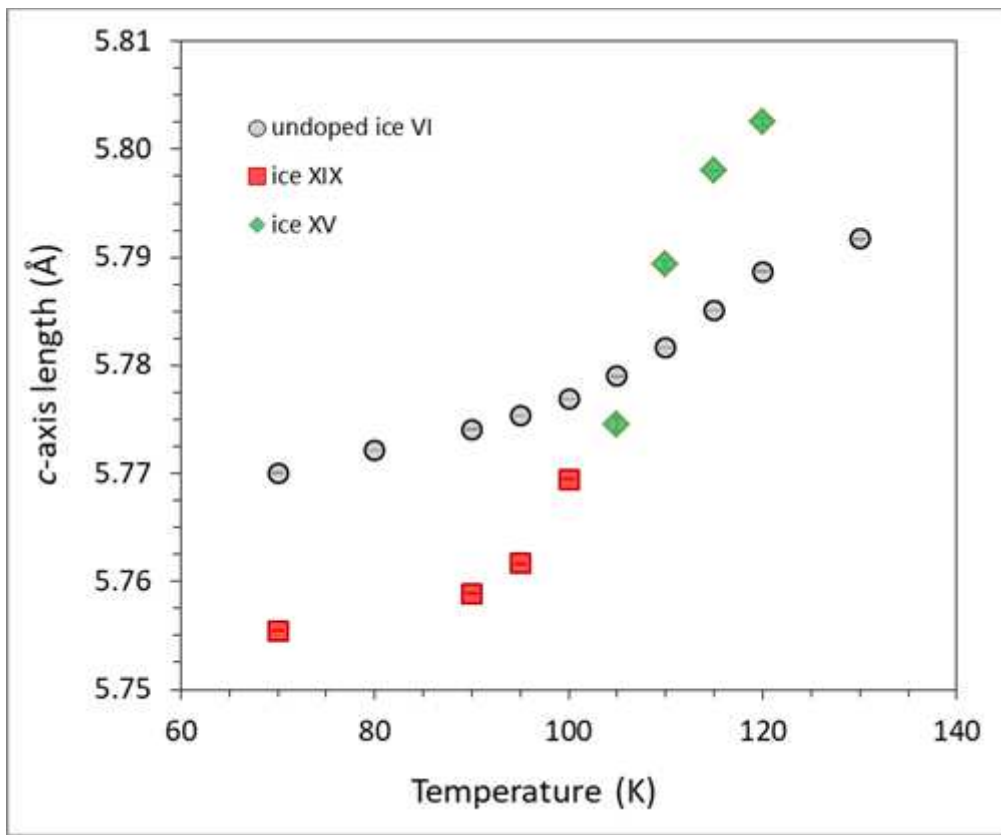


Figure 4

Change in c-axis length upon heating ice XIX (red squares and green diamonds, obtained from Rietveld refinement of the data set shown in Figure 3) compared with a heating scan of undoped ice VI (circles).

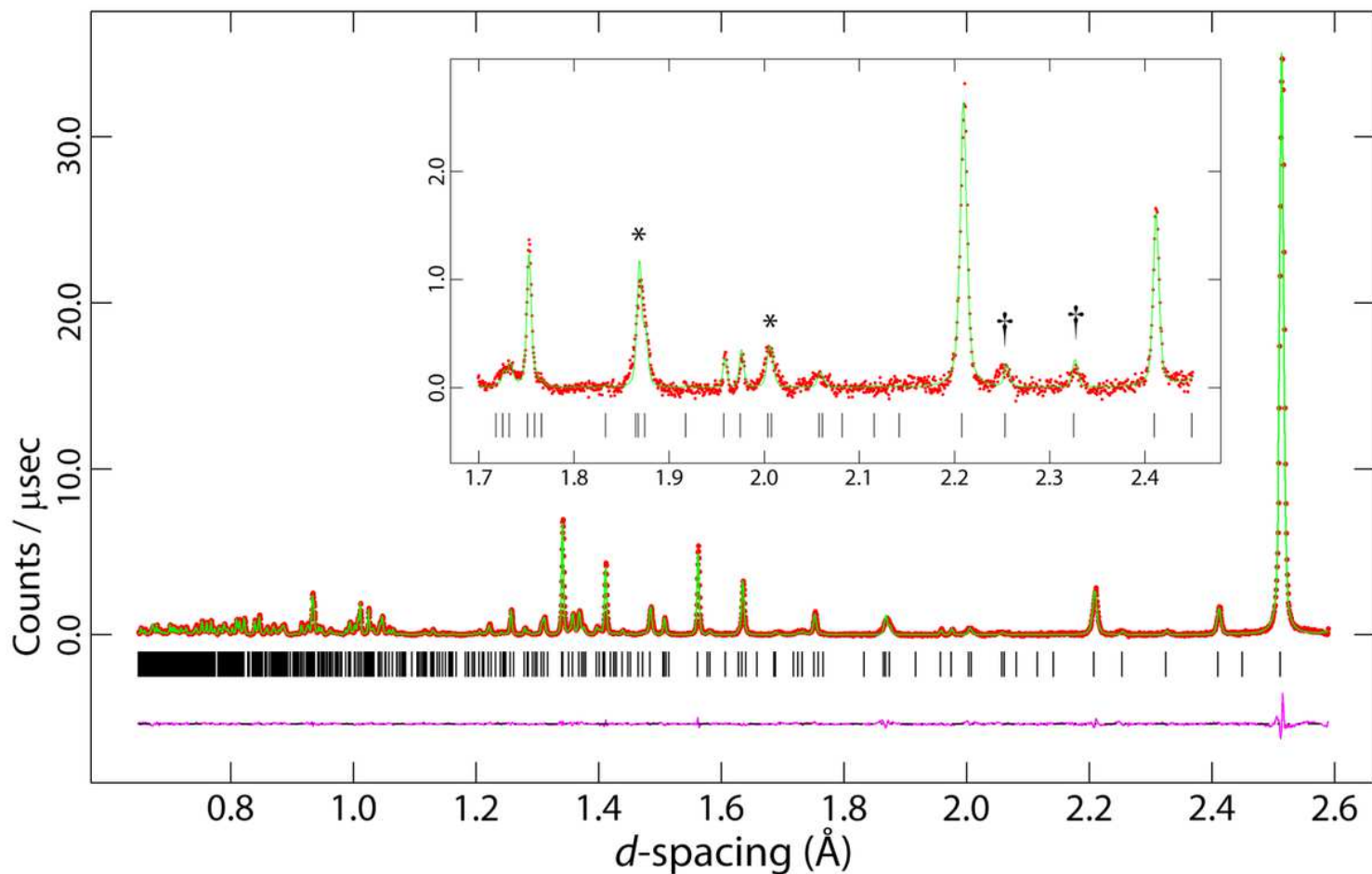


Figure 5

Neutron powder diffraction data for ice XIX (red circular symbols) and the fit calculated from the refined P4 \times model (green line), with the background subtracted. The difference between the model and data is represented by the purple line underneath the diffraction pattern, and the positions of the Bragg peaks are indicated by vertical black tick marks. The inset shows the region between 1.7 and 2.45 Å d-spacing where peaks appear that are permitted by the ice VI cell metric but have little or no intensity in ice VI (*) and where super-lattice peaks are observed (†).

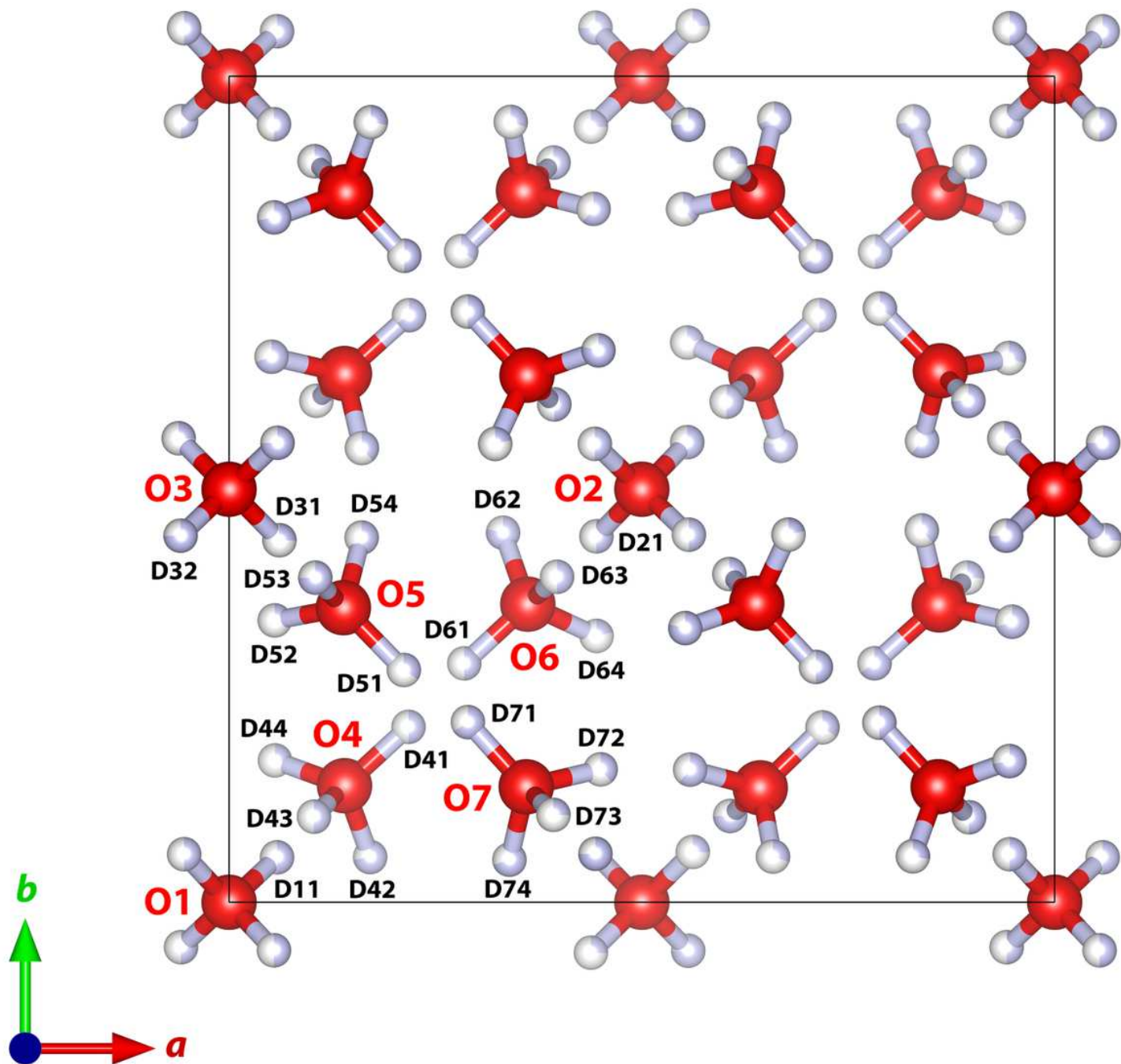


Figure 6

Unit-cell of ice XIX (refined P4 \times model) viewed along the c-axis, showing the atom labelling scheme used in Table 1. Shading of the hydrogen atoms indicates the occupancy, reported quantitatively in Table 1.